Testing the Trade Wind Charging Mechanism and Its Influence on ENSO Variability

SOUMI CHAKRAVORTY,[a,b] RENELLYS C. PEREZ,[b] BRUCE T. ANDERSON,[c] BENJAMIN S. GIESE,[d] SARAH M. LARSON,[e] AND VALENTINA PIVOTTI[c]

[a] *Cooperative Institute of Marine and Atmospheric Studies, University of Miami, Miami, Florida*
[b] *NOAA Atlantic Oceanographic and Meteorological Laboratory, Miami, Florida*
[c] *Department of Earth and Environment, Boston University, Boston, Massachusetts*
[d] *Department of Oceanography, Texas A&M University, College Station, Texas*
[e] *Department of Marine, Earth, and Atmospheric Sciences, North Carolina State University, Raleigh, North Carolina*

(Manuscript received 27 September 2019, in final form 29 May 2020)

ABSTRACT

During the positive phase of the North Pacific Oscillation, westerly wind anomalies over the subtropical North Pacific substantially increase subsurface heat content along the equator by ''trade wind charging'' (TWC). TWC provides a direct pathway between extratropical atmospheric circulation and El Niño–Southern Oscillation (ENSO) initiation. Previous model studies of this mechanism lacked the ocean–atmospheric coupling needed for ENSO growth, so it is crucial to examine whether TWC-induced heat content anomalies develop into ENSO events in a coupled model. Here, coupled model experiments, forced with TWC favorable (+TWC) or unfavorable (−TWC) wind stress, are used to examine the ENSO response to TWC. The forcing is imposed on the ocean component of the model through the first winter and then the model evolves in a fully coupled configuration through the following winter. The +TWC (−TWC) forcing consistently charges (discharges) the equatorial Pacific in spring and generates positive (negative) subsurface temperature anomalies. These subsurface temperature anomalies advect eastward and upward along the equatorial thermocline and emerge as like-signed sea surface temperature (SST) anomalies in the eastern Pacific, creating favorable conditions upon which coupled air–sea feedback can act. During the fully coupled stage, warm SST anomalies in +TWC forced simulations are amplified by coupled feedbacks and lead to El Niño events. However, while −TWC forcing results in cool SST anomalies, pre-existing warm SST anomalies in the far eastern equatorial Pacific persist and induce local westerly wind anomalies that prevent consistent development of La Niña conditions. While the TWC mechanism provides adequate equatorial heat content to fuel ENSO development, other factors also play a role in determining whether an ENSO event develops.

1. Introduction

El Niño–Southern Oscillation (ENSO) describes the irregular 2–7-yr variability in the state of the ocean and atmosphere in the tropical Pacific (Rasmusson and Carpenter 1982; Philander 1983, 1990; Wyrtki 1985; Jin 1997; Li 1997). Given the far-reaching impact of ENSO on global weather and climate (e.g., Alexander 1992; Lau and Nath 1996; Wang et al. 2000; Yuan 2004; McPhaden et al. 2006; Yeh et al. 2014; Zhou et al. 2014; Min et al. 2015; Chakravorty et al. 2013, 2016), improving the accuracy of ENSO predictions has been a long-standing goal in climate research. ENSO prediction skill has increased over the past several decades because of improved understanding of the coupled oceanic–atmospheric processes underlying the ENSO phenomenon, as facilitated by knowledge obtained from the tropical Pacific observing system, improvements in models, and data assimilation systems (e.g., McPhaden et al. 1998; Guilyardi et al. 2009; Barnston et al. 2012). Yet, there is still considerable uncertainty regarding which processes are crucial to further improve ENSO prediction skill at long lead times (Tippett et al. 2012).

Although ENSO is a tropical phenomenon, the extratropics have also been shown to impact ENSO variability (Chiang and Vimont 2004; Chang et al. 2007; Vimont et al. 2009) and recent work suggests that incorrect prediction of extratropical precursors may contribute to ENSO forecast uncertainty (Larson et al. 2018a). Therefore, improved understanding of the physical mechanisms by which extratropical precursors impact

Corresponding author: Soumi Chakravorty, soumi.chakravorty@noaa.gov

DOI: 10.1175/JCLI-D-19-0727.1

the equatorial Pacific may be vital to improving ENSO predictions. Numerous studies suggest a robust relationship between midlatitude atmospheric variability and the development of ENSO (e.g., Pierce et al. 2000; Anderson 2003, 2004, 2007; Anderson et al. 2017; Vimont et al. 2003a,b). Of particular importance is the North Pacific Oscillation (NPO; Rogers 1981; Linkin and Nigam 2008), which is the second leading mode of atmospheric variability during boreal winter (November–January). In its positive phase, the NPO is characterized by a high sea level pressure (SLP) anomaly centered near 60°N and a low SLP anomaly centered near 35°N and can influence tropical variability through both oceanic and atmospheric processes (Vimont et al. 2001, 2003a,b; Anderson 2003, 2004, 2007; Chiang and Vimont 2004; Chang et al. 2007; Alexander et al. 2010).

Several mechanisms have been proposed to explain how the NPO can influence ENSO events. In one scenario, during the positive phase of the NPO, the southern lobe of the SLP dipole induced anomalous westerly winds over the central and eastern subtropical North Pacific, which oppose the prevailing easterly trade winds. This acts to reduce evaporative cooling of the ocean, leaving a warm SST "footprint" in the subtropics (Vimont et al. 2003a,b). This SST footprint, a hallmark of the North Pacific meridional mode (NPMM; Chiang and Vimont 2004), persists until the following summer and further modifies the overlying atmospheric pressure and wind fields through the positive wind–evaporation–SST (WES) feedback (Xie and Philander 1994). This results in an anomalous meridional SST gradient over the central tropical Pacific (Liu and Xie 1994; Vimont 2010; Wang 2010) that can drive a latitudinal shift of the intertropical convergence zone (ITCZ), weaken the equatorial easterlies, and trigger the onset of El Niño events (Alexander et al. 2010; Chang et al. 2007; Larson and Kirtman 2013, 2014). The reverse process operates during the negative NPO phase and can trigger a cold ENSO event, or La Niña (Alexander et al. 2010). Importantly, according to these arguments, NPO anomalies communicate to the tropics only through thermodynamic processes (Xie and Philander 1994; Chang et al. 2007; Vimont 2010).

However, there is an alternative, dynamically based paradigm for the communication of the NPO to the tropics, termed the "trade wind charging" (TWC) mechanism (Anderson 2007; Anderson et al. 2013; Anderson and Perez 2015). As part of the TWC mechanism, the southern lobe of the positive NPO–related SLP anomalies generates westerly wind stress anomalies that extend from the western tropical Pacific into the subtropical North Pacific, accompanied by easterly wind stress anomalies over the eastern equatorial Pacific. These wind anomalies result in an off-equatorial wind stress curl that drives an equatorward mass transport, thereby priming the system for an ENSO event (Anderson 2007; Anderson et al. 2013; Anderson and Perez 2015). Although the TWC wind patterns are similar to those associated with the seasonal footprint mechanism (SFM; Vimont et al. 2003a,b) and NPMM processes (Anderson and Perez 2015), the TWC mechanism provides a more direct pathway between extratropical atmospheric circulation and ENSO event initiation. In this case, ocean dynamics play a critical role in charging of central equatorial Pacific subsurface heat content, resulting in increased warm water volume (WWV), a well-known ENSO precursor (Wyrtki 1985; Jin 1997; Meinen and McPhaden 2000; Wen et al. 2014). Importantly, heat content buildup associated with the TWC mechanism is a consequence of ocean adjustment to off-equatorial winds and is independent of ENSO (Anderson 2003, 2004). Therefore, it is distinctly different from the traditional recharge/discharge (Jin 1997) related changes in WWV that are a consequence of the ocean adjustment to equatorial winds related to the preceding ENSO phase.

While observational results reveal empirical and dynamical links between NPO-induced modification of the North Pacific trade winds and concurrent basin-scale tropical Pacific heat content changes, most of the coupled model studies to date have focused on the thermodynamic influence of NPO-related trade wind variations on ENSO (e.g., NPMM/SFM). Previous experiments using a high-resolution ocean-only model reveal that positive NPO–related trade wind variations induce the charging of subsurface heat in the central Pacific (Anderson et al. 2013; Anderson and Perez 2015). The experiments show that these warm subsurface temperature anomalies advect eastward and generate a warming of eastern equatorial Pacific SST (Anderson et al. 2013; Anderson and Perez 2015). However, ocean-only models are unable to amplify the positive SST anomalies in the eastern equatorial Pacific because they lack ocean–atmosphere coupling [i.e., the Bjerknes (1969) feedback mechanism]. As a result, it has yet to be shown whether TWC-induced equatorial heat content and the associated eastern equatorial Pacific SST anomalies can subsequently develop into mature ENSO events in a coupled model setting.

In this study, we test the efficacy of the TWC mechanism on ENSO variability using a coupled model experimental framework that provides opportunity for TWC-induced equatorial anomalies to evolve into mature ENSO events. Details of the controlled model framework and experimental design are provided in section 2. The results, obtained from different sensitivity experiments, are presented in sections 3 and 4, and a

summary of the key results and conclusions is provided in section 5.

2. Coupled model framework and the experimental setup

a. Model description

The coupled model used in this study is the National Center for Atmospheric Research (NCAR) Community Earth System Model version 1.2.2.1 (CESM1; Hurrell et al. 2013). This version of the model is configured with the Parallel Ocean Program version 2 ocean model (POP2; Smith et al. 2010) and is coupled to the Community Atmosphere Model version 5 (CAM5; Gettelman et al. 2010; Neale et al. 2012). These model components communicate with each other through the CESM flux coupler version 7, which computes air–sea fluxes using the Large and Yeager (2009) surface layer scheme. The ocean receives the flux information from the coupler once per model day. POP2 is run with a nominal 1° horizontal resolution, with finer meridional resolution, approximately 0.3° latitude, near the equator. The ocean model has 60 vertical z levels, with a vertical resolution of 10-m increments in the upper 160 m of the ocean (Danabasoglu et al. 2012). The CAM5 model has a horizontal resolution of 0.9° latitude × 1.25° longitude, and 30 vertical layers arranged in a hybrid pressure sigma coordinate.

CESM1 simulates realistic ENSO events with a periodicity of 2–7 years and seasonal phase-locking (DiNezio et al. 2017; Wieners et al. 2019). However, it overestimates the SST variability associated with ENSO by about 50% (DiNezio et al. 2017). CESM1 has improved representation of the asymmetry in the strength and frequency of El Niño versus La Niña events compared with previous versions of the model, although it still underestimates the observed El Niño/La Niña asymmetry (DiNezio et al. 2017; Zhang et al. 2017).

b. Experimental setup

We employ an idealized two-step model framework (by transitioning from a forced version of CESM1 in which the atmosphere's communication with the ocean is manually controlled to the fully coupled version of CESM1) to highlight the effect of TWC forcing on ENSO evolution. As both the initial and boundary conditions have a strong influence on ENSO's evolution, in the first step of the experimental design the coupled model is integrated in a "controlled flux stage" to minimize these influences and isolate the ocean's response to the TWC mechanism. In the second step, the coupled model is integrated in a "fully coupled stage" during which any TWC-induced tropical signals have the opportunity to amplify and evolve into mature ENSO events.

1) Controlled flux stage

For the controlled flux stage, we choose initial conditions that minimize the presence of equatorial oceanic heat content anomalies in the initial ocean conditions, as they can significantly impact the distribution of ENSO outcomes in ensemble model experiments (e.g., Larson and Kirtman 2019). These initial conditions originate from a 222-yr fully coupled control simulation (CTL) of CESM1, integrated from a 500-yr spinup run with preindustrial (1850) radiative forcing.

As the ensemble experiments are initialized on 1 November [hereafter 1 Nov(0); other months are similarly styled], we select all 1 Nov(0) initial conditions from the CTL simulation that 1) are in an ENSO-neutral state to begin with and 2) have a tendency to remain ENSO-neutral over the following 12–14 months. This is achieved by applying the following two criteria. First, the monthly average Niño-3.4 SST anomaly in Nov(0) must be within the range of ±0.5°C (to ensure that near-neutral conditions exist in the equatorial Pacific SST). Second, the Niño-3.4 SST anomaly one year later, during the subsequent winter Nov(1)–Jan(2) [NDJ(1/2)], must be within the range of ±1°C (to ensure the absence of any precursor conditions in the initial ocean state that could result in the development of a mature ENSO event the following year). A total of 31 branch points satisfies the above criteria and are selected as initial conditions for the ensemble experiments.

Figure 1 shows the monthly averaged Niño-3.4 SST anomaly from the 222-yr CTL simulation of CESM1. Comparison with the center of heat index (CHI; Ray and Giese 2012; not shown), which allows the longitudinal center of SST anomalies to vary as a function of time and hence is not geographically fixed, indicates that the Niño-3.4 SST index is an appropriate indicator of ENSO variability in this model (i.e., ENSO warming is typically centered within the longitudinal range of the Niño-3.4 box) and thus this index is used throughout the rest of the analysis. The vertical black lines in Fig. 1 identify the Nov(0) branch points for the 31 years selected as the initial conditions for the ensemble experiments and the gray shaded areas highlight their evolution in the CTL simulation up to the end of Dec(1).

Figure 2a compares the temporal evolution of the Niño-3.4 SST anomalies from Nov(0) to Dec(1) for these selected years (black lines) with all other years in the CTL (gray lines). This confirms that during the selected years, the surface conditions remain relatively ENSO-neutral throughout their evolution. The scatterplot between the initial Niño-3.4 anomalies and the average Niño-3.4 anomalies of the following winter

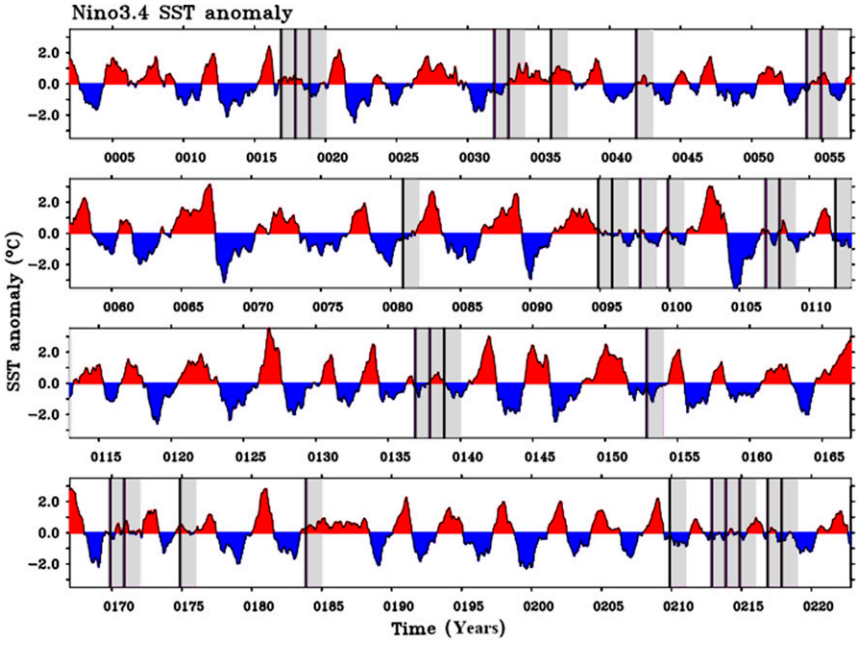

FIG. 1. Monthly mean Niño-3.4 SST (°C) anomaly with 3-month smoothing calculated from the 222-yr preindustrial fully coupled (CTL) simulation. The black vertical lines show the selected Nov(0) branch points that serve as neutral initial conditions for the controlled flux experiments and the gray shaded areas highlight their evolution in the CTL simulation during the following year.

show a clustering of points near the origin for the selected events (black dots in Fig. 2c) further illustrating the near-neutral ENSO conditions. Similarly, the WWV anomalies (computed as the integrated volume above the 20°C isotherm in the region 5°N–5°S, 120°E–80°W) for the selected years confirm that subsurface heat content along the equatorial Pacific is relatively ENSO-neutral during the initial state (black dots in Fig. 2d) and remains fairly neutral throughout the evolution (black lines in Fig. 2b).

To control for the atmospheric boundary conditions so as to isolate the dynamical influence of the TWC mechanism, we force the ocean component of the model with TWC-related wind stress anomalies (see section 2c) superimposed onto the climatological wind stress (calculated from the ~50 years of the CTL simulation for which the daily values of heat and momentum fluxes were archived). This is referred to as a mechanically decoupled version of the model [see Larson et al. (2018b) for more details] and, by design, deactivates wind-driven coupled feedbacks (e.g., the Bjerknes feedback) and removes the dynamic impact of atmospheric noise (e.g., wind bursts) on the ocean (Larson and Kirtman 2015). In our experimental setup, the ocean can only dynamically respond to the prescribed wind stress, which by design (the absence of strong wind anomalies over eastern equatorial Pacific) does not allow the model SSTs to grow into mature ENSO events. Further, to eliminate thermodynamic influences of the boundary conditions on SST via thermally coupled modes such as NPMM and SFM, we also disconnect the thermodynamic coupling in CESM1. This is done by forcing the ocean model with prescribed climatological thermal (and freshwater) fluxes (again, calculated from the ~50 years of the CTL simulation for which the daily values of heat and momentum fluxes were archived) during the controlled flux stage. During this stage the atmosphere remains unconstrained and freely responds to the underlying ocean state but the reverse feedback is disabled.

2) FULLY COUPLED STAGE

In the fully coupled stage of the modeling framework, we remove all the flux constraints beginning on 1 Aug(1) and allow the system to freely evolve on its own under the fully coupled configuration. During this stage, TWC-generated SST anomalies in the eastern equatorial Pacific have the opportunity to grow via coupled air–sea feedbacks and evolve into ENSO events.

c. *Ensemble experiments*

To isolate the effect of TWC wind stress forcing on ENSO evolution, we perform three ensemble experiments, each of which contains 31 ensemble members initialized from the 31 initial Nov(0) states identified in section 2b(1). The ensemble approach is necessary to

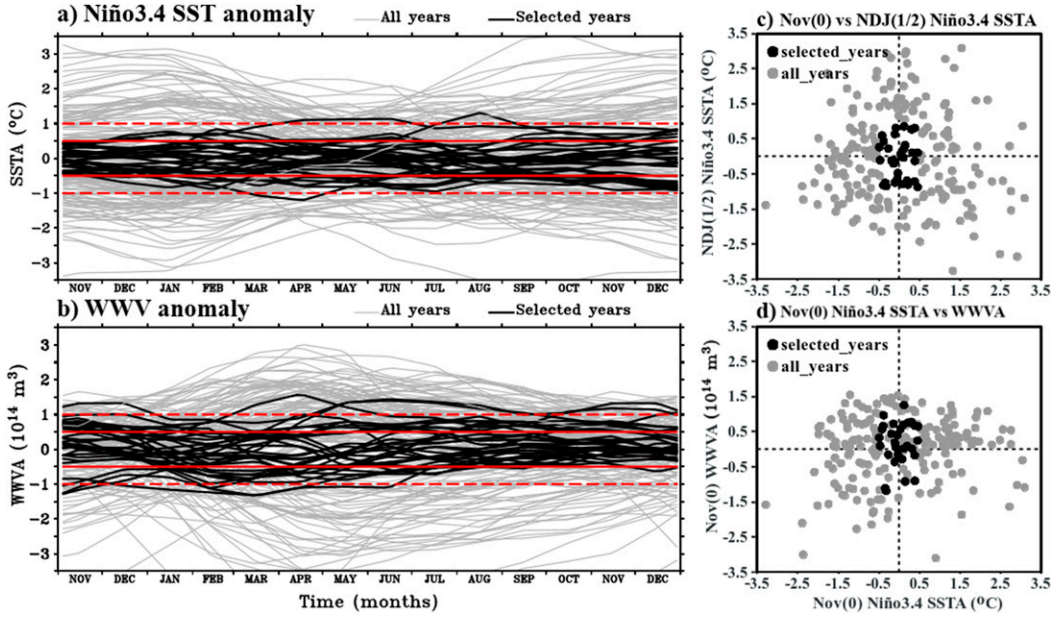

FIG. 2. Evolution of monthly mean (a) Niño-3.4 SST anomalies (°C) and (b) WWV anomalies (10^{14} m^3) with 3-month smoothing and averaged over the equatorial Pacific (120°E–80°W, 5°S–5°N) from Nov(0) to Dec(1) for the CTL simulation (gray lines). The 31 selected neutral years are indicated by black lines, and solid (dashed) red lines show anomalies of ±0.5°C (±1°C) for Niño-3.4 SST anomalies (SSTA) and ±0.5 × 10^{14} m^3 (±1 × 10^{14} m^3) for WWV anomalies (WWVA). (c) Scatterplot of the Nov(0) vs NDJ(1/2) Niño-3.4 SSTA for the CTL simulation (gray dots) and 31 neutral years (black dots). (d) As in (c), but for concurrent Niño-3.4 SSTA vs WWVA in Nov(0).

isolate the mean response to the TWC mechanism, as internal variability generates a large ENSO spread after coupling has been reintroduced (Larson and Kirtman 2015).

1) THE +TWC ENSEMBLE

The +TWC ensemble is generated by forcing the model (during the controlled flux stage) with +TWC-related wind stress anomalies (associated with the positive phase of the NPO) superimposed on the climatological wind stress fields. The NPO, and hence TWC mechanism, is generally weak in CESM1 and the typical structure of the NPO pattern is not well represented (Thomas and Vimont 2016; Chen et al. 2018). For this reason, +TWC-related wind stress anomaly fields are reconstructed using the observationally constrained 20CRv2c momentum fluxes and SST from the SODAsi.3 reanalysis product (Carton and Giese 2008; Giese et al. 2016), which has a realistic ENSO (Giese and Ray 2011; Ray and Giese 2012) and manifests the TWC mechanism (Anderson et al. 2013). Details regarding the identification and isolation of the observationally constrained TWC-related wind stress fields can be found in the appendix. One point to emphasize here is that, following the lead of previous analyses, we constrain these TWC-related wind stress fields to be independent of the ENSO cycle (see the appendix for details).

To impose these +TWC-related wind stress anomalies (Fig. 3a), the so-called controlled flux stage is divided into two intervals (Figs. 3b,c): 1) the anomaly forced interval during which the ocean is forced by +TWC anomalies (added to the climatological wind stress fields) applied from 1 Nov(0) to 30 Apr(1), as the TWC-related wind pattern is prevalent during boreal winter; and 2) the climatology forced interval during which the ocean is forced by climatological wind stresses applied from 1 May(1) to 31 Jul(1). During the anomaly-forced interval, +TWC anomalies are ramped up over the first month and ramped down in the last month. The fully coupled stage then begins on 1 Aug(1), after which the model is integrated for the next 8 months until 31 Mar(2) (Figs. 3b,c).

2) THE NOTWC ENSEMBLE

We perform an ensemble experiment in which the ocean is forced with only climatological wind stress during the entire controlled flux stage (both intervals), hereafter called the NoTWC ensemble. The NoTWC ensemble is designed in such a way that all coupled variability is suppressed in the initial controlled flux stage. In the subsequent fully coupled stage, ENSO events can develop but only due to the model's internal variability. Thus, this ensemble provides an estimate for the internally generated spread of ENSO that can occur from an ENSO-neutral state in CESM1 and thus

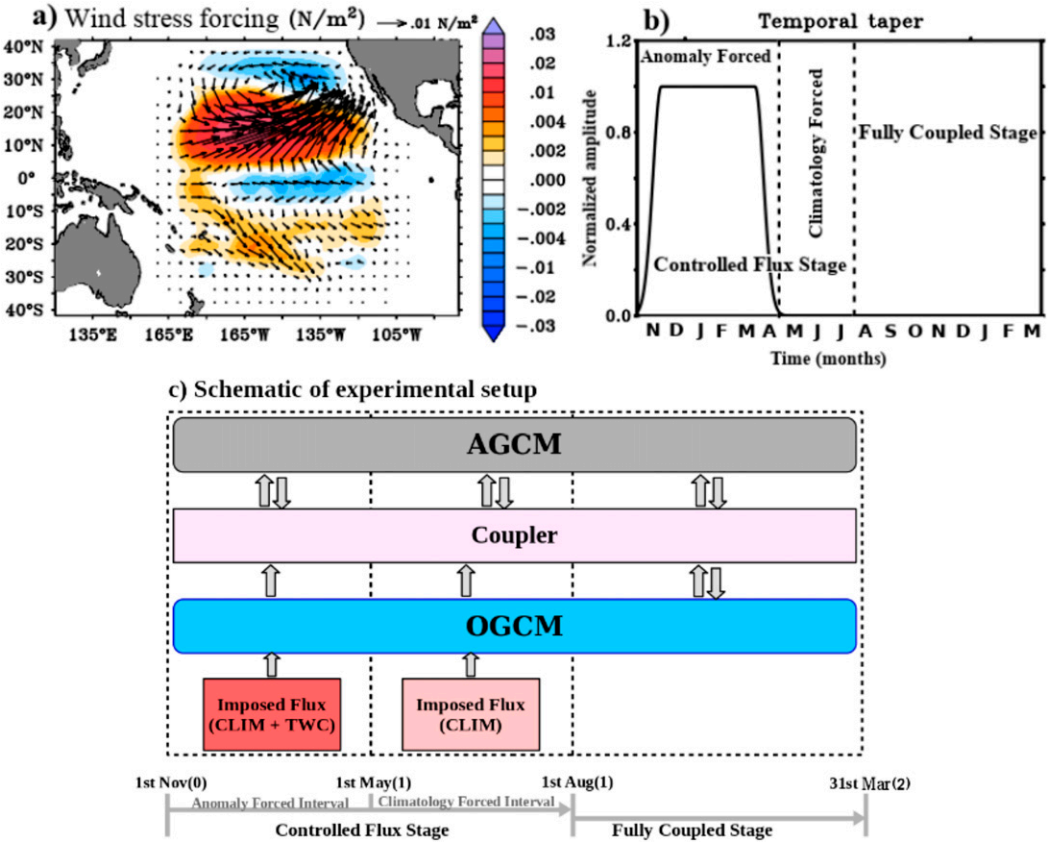

FIG. 3. (a) The spatial pattern of wind stress forcing added to the climatological forcing and applied to each ensemble member during the controlled flux stage of the +TWC experiment. Total wind stress anomalies (N m^{-2}; vectors) are scaled to the reference vector at the top-right corner; zonal wind stress anomalies (N m^{-2}; shaded) correspond to the color bar to the right of the panel. (b) Time evolution of the forcing applied during the controlled flux stage (from November of year 0 to July of year 1) and the fully coupled stage of the +TWC experiment (from August of year 1 to March of year 2). For the −TWC experiment, the anomaly forcing is simply reversed in sign; for the NoTWC experiment, the anomaly forcing amplitude is "0" at all times from November of year 0 to July of year 1. (c) Schematic of the model experimental setup.

provides an essential baseline to compare with the other ensembles.

3) THE −TWC ENSEMBLE

Last, to determine whether tropical Pacific variability is symmetrically responsive to positive versus negative TWC forcing, we conduct a −TWC ensemble experiment in which the anomalous wind stress forcing is the opposite sign of that shown in Fig. 3a. This ensures that any differences in ENSO response are not the result of structural differences in the forcing itself.

3. Analysis of ensemble experiments

a. NoTWC ensemble results

As described in the previous section, we integrate the NoTWC experiment in such a way that coupled variability in the ocean is eliminated during the controlled flux stage. Figure 4a shows the evolution of 5-day averaged Niño-3.4 SST from Nov(0) to Mar(2) for each member of the NoTWC experiment (gray lines) as compared with the climatological evolution of Niño-3.4 SST generated from the last 50 years of the CTL (pink line). The NoTWC ensemble mean (black line) agrees well with the CTL climatology, although NoTWC is slightly warmer during the summer of year 1 (i.e., near the end of the controlled flux stage). The ensemble spread is very small during the controlled flux stage [e.g., blue vertical bar in Jul(1) in Fig. 4a]. Once the flux constraint is removed and the model begins to evolve freely in a fully coupled fashion from 1 Aug(1) onward, the ensemble spread increases due to the model's internal variability but remains narrower than the variability exhibited by the CTL (cf. blue and pink vertical bars). Figure 4b shows the corresponding equatorial Pacific WWV time series, a proxy for heat content, for

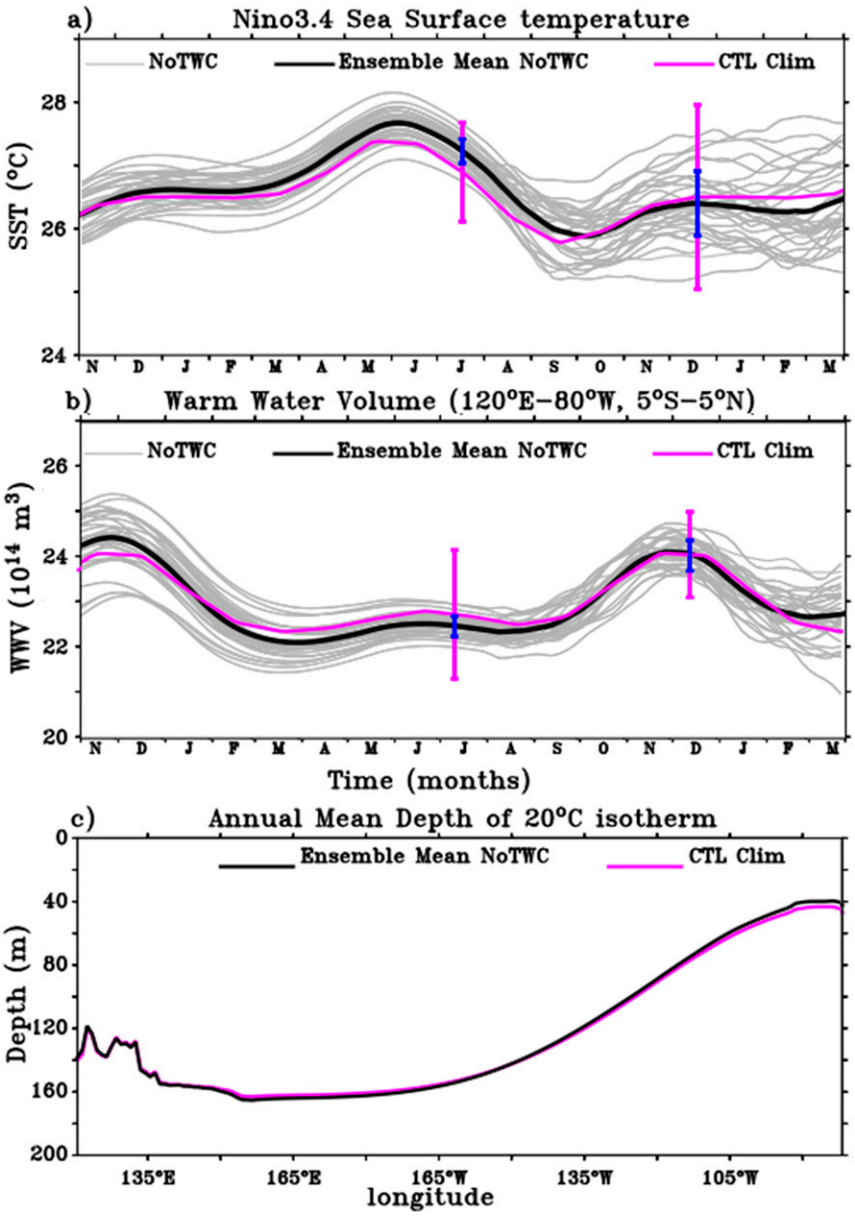

FIG. 4. Evolution of 5-day means of (a) Niño-3.4 SST (°C) and (b) WWV (10^{14} m^3) with 3-month smoothing and averaged over 120°E–80°W, 5°N–5°S from Nov(0) to Mar(2) for NoTWC ensemble members (gray lines) and the ensemble mean (black line). The pink continuous line shows the climatological mean from years 175 to 222 of the CTL simulation. The pink vertical lines show the spread of the CTL simulation about the climatological mean for Jul(1) and NDJ(1/2). The blue vertical lines are same as the pink, but for the NoTWC ensembles. Ensemble spread is calculated as the standard deviation of the ensemble members (c) Annual mean depth of the 20°C isotherm (D20; m) averaged over 5°S–5°N as a function of longitude for the NoTWC ensemble mean (black line) and the CTL climatology (pink line).

the individual NoTWC members (gray lines) and the ensemble mean (black line). The close proximity of the ensemble mean WWV to the CTL climatology (pink line in Fig. 4b) and the narrow ensemble spread (even after coupling is turned on) suggests the absence of strong subsurface variability in the individual ensemble members (blue vertical bars in Fig. 4b). In Fig. 4c, the similarity of the annual mean zonal thermocline depth in the NoTWC ensemble mean (black line) with the CTL ensemble mean (pink line) further confirms that

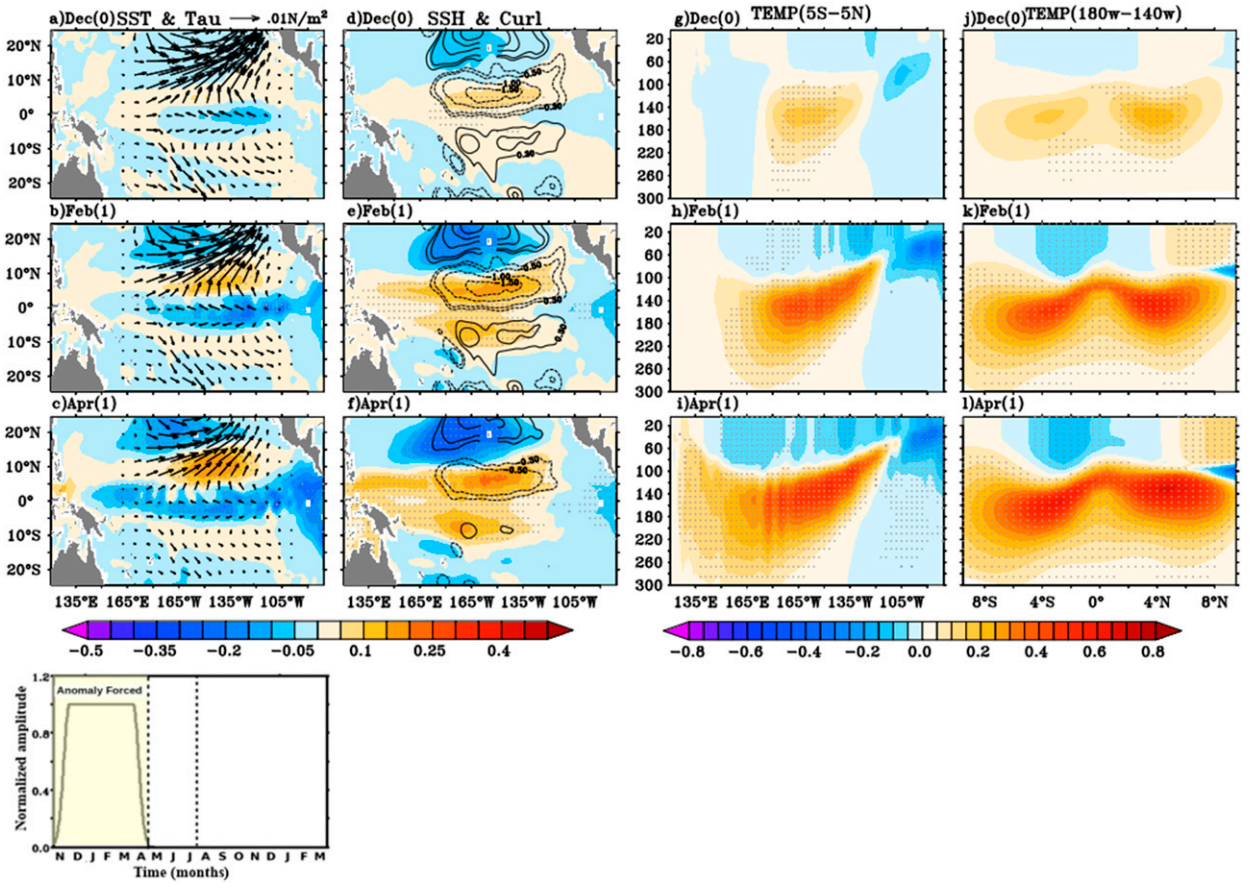

FIG. 5. Ensemble mean model response to +TWC wind stress forcing during the anomaly-forced interval of the controlled flux stage in Dec(0), Feb(1), and Apr(1). The difference between +TWC and NoTWC ensemble means are shown for (a)–(c) SST (°C; shaded) and wind stress (tau; N m^{-2}, vectors) scaled to the reference vector at the top-right corner, (d)–(f) SSH (m; shaded) and wind stress curl (10^{-8} N m^{-3}; contours with values ±0.3, ±0.5, ±1, ±1.5, and ±2), (g)–(i) meridionally averaged (5°N–5°S) temperature anomalies, and (j)–(l) zonally averaged (180° to 140°W) temperature anomalies (°C), designated by color bar at the bottom of the panels. Stippling indicates regions where the ensemble mean differences are significant with 90% confidence based on a two-tailed Student's *t* test. The bottom panel highlights the corresponding timing relative to the 17-month +TWC experiment.

climatological forcing adequately reproduces the mean thermocline depth from the fully coupled CTL. Thus, the prescribed climatological fluxes do not unintentionally bias the mean state and the NoTWC ensemble is an appropriate analog for neutral conditions in the equatorial Pacific and can be used as a baseline for our sensitivity experiments.

b. +TWC ensemble results

1) VERIFICATION OF THE TWC MECHANISM

According to the TWC mechanism, there are three hypothesized responses to imposed +TWC wind stress forcing: 1) an initial charging of the central equatorial Pacific with subsurface heat content almost concurrent with the wind stress forcing; 2) an eastward migration of this subsurface heat content anomaly along the equatorial thermocline, resulting in the emergence of like-signed eastern equatorial Pacific SST anomalies; and finally, 3) the development and maturation of El Niño conditions across the equatorial Pacific following the emergence of the eastern equatorial Pacific SST anomalies. In the following we test each of these hypothesized responses at various intervals within the controlled flux and fully coupled stages of the +TWC experiment.

2) ANOMALY FORCED INTERVAL

Here we aim to examine how effective the +TWC forcing, in isolation, is at charging the equatorial Pacific with positive subsurface ocean heat content. Figure 5 depicts the evolution of the tropical Pacific during the +TWC anomaly forced interval of the controlled flux stage by showing the ensemble mean difference between the +TWC and NoTWC simulations. These differences

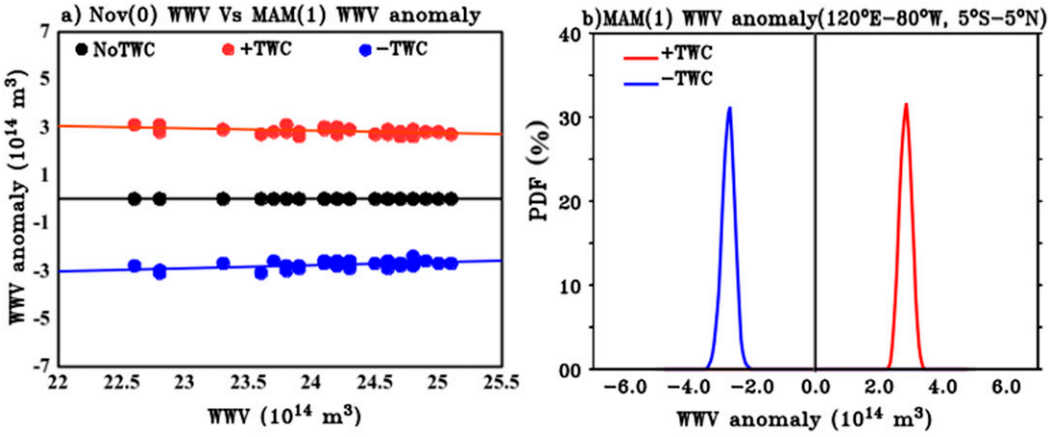

FIG. 6. (a) Scatterplot of the Nov(0) WWV (10^{14} m^3) vs March–May year 1 [MAM(1)] WWV anomalies (10^{14} m^3) for the 31 ensemble members (averaged over 120°E–80°W, 5°N–5°S). For each ensemble member, MAM(1) WWV anomalies are computed relative to the corresponding NoTWC WWV value. Black dots correspond to the NoTWC ensembles (and by construction are identically zero), red dots correspond to the +TWC ensembles, and blue dots correspond to the −TWC ensembles. (b) Probability density function (PDF; %) of the MAM(1) WWV anomalies for the +TWC (red) and −TWC (blue) ensembles.

reveal the direct response of the tropical Pacific Ocean to the imposed anomalous wind stress forcing. Ensemble mean differences in SST, sea surface height (SSH; as a proxy of thermocline depth), wind stress, wind stress curl, and subsurface temperature anomalies are shown for Dec(0), Feb(1), and Apr(1).

The initial ocean response to imposed +TWC forcing is present in the off-equatorial central Pacific SSH anomalies (Fig. 5d) accompanying significant deepening of the thermocline. In this region, the imposed off-equatorial westerly wind stress anomalies act to weaken the prevailing trade winds, which when combined with anomalous equatorial easterlies generate off-equatorial anticyclonic curl (black contours in Figs. 5d,e) in the central Pacific that induces downward Ekman pumping and thus displaces the thermocline downward. Importantly, the anticyclonic wind stress curl in the central equatorial Pacific is accompanied by equatorward vertically integrated mass transport [consistent with Clarke et al. (2007) and Anderson and Perez (2015)]. Hence as the forcing persists, there is a subsequent increase in SSH (Figs. 5e,f) and subsurface temperatures along the equator (Figs. 5h,i), representative of a ''charged'' equatorial Pacific. Cross-equatorial sections of temperature in the central Pacific (Figs. 5j–l) clearly indicate that the formation of positive subsurface temperature anomalies initially takes place along the thermoclines near 5°N and 5°S, which then subsequently move equatorward. Along the equator, subsurface temperature anomalies remain relatively stationary (Figs. 5h,i); however, off the equator SSH (and by extension subsurface temperature) anomalies show a westward propagation (Figs. 5e,f), suggestive of an off-equatorial baroclinic Rossby wave response to the +TWC wind stress forcing. Despite the absence of surface heat flux anomalies (by design), there is a surface temperature response to the +TWC wind stress forcing, including a cooling along the equator and a warming of the off-equatorial central North Pacific (Figs. 5a–c). Cooling at the equator is the result of enhanced easterly trade winds that drive shoaling of the thermocline and more vigorous mixing in the oceanic boundary layer, whereas warming of the off-equatorial central North Pacific is in response to weakened easterly trades that results in a deepening of the thermocline (discussed above) and weaker mixing.

Based on this analysis, it is evident that +TWC forcing increases subsurface heat content and thus charges the equatorial central Pacific with warm water consistent with previous studies (Anderson 2004; Anderson and Maloney 2006). These warming conditions can serve as a potential precursor for El Niño events. Scatterplots of the Nov(0) WWV versus the Mar(1)–May(1) [MAM(1)] WWV anomalies across the equatorial Pacific are shown in Fig. 6a for the individual ensemble members of NoTWC (black dots), +TWC (red dots), and −TWC (blue dots) ensembles. For each ensemble member, anomalies are computed with respect to the corresponding NoTWC ensemble member that starts from the same initial condition; thus, the NoTWC ensembles by construction have a value of zero. The robustness of the buildup of subsurface heat content in response to the +TWC anomaly is clearly evident (red dots). The approximately 2.9 × 10^{14} m^3 increase of WWV

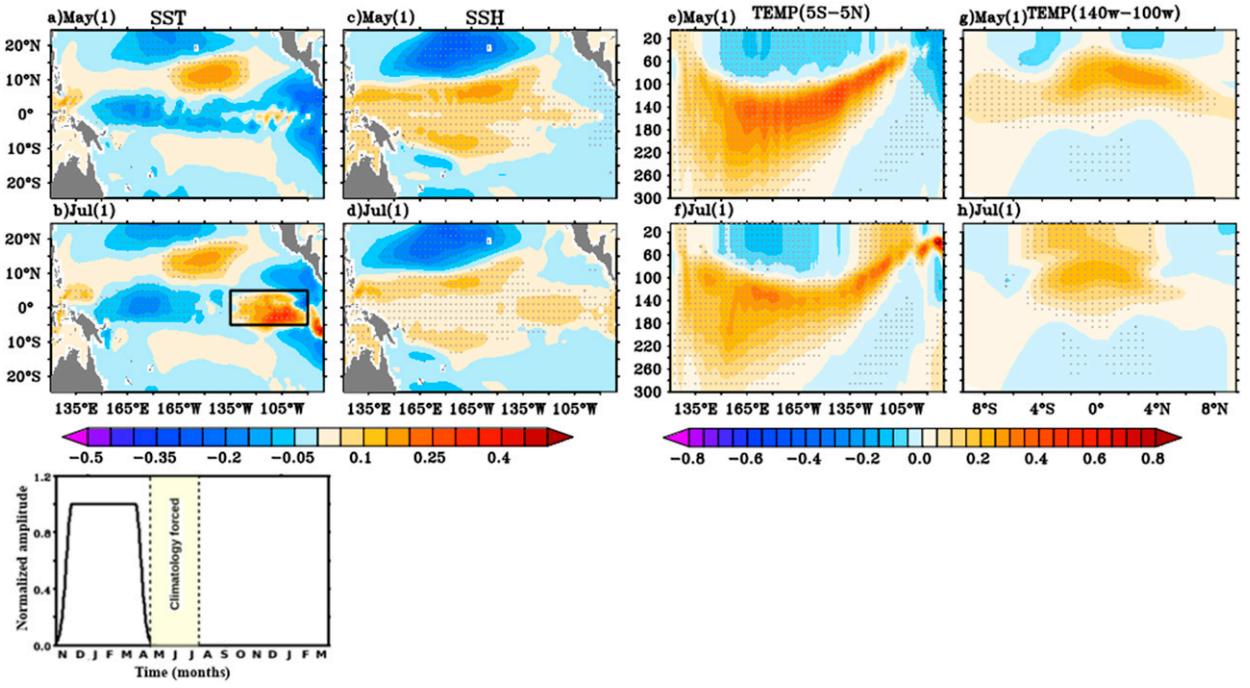

FIG. 7. As in Fig. 5, but for the +TWC ensemble mean response during the climatology-forced interval of the controlled flux stage in May(1) and Jul(1). Ensemble mean differences of wind stress and curl during this time period are by construction zero, and hence are not shown. The black box in (b) indicates the ENSO onset region (135°–90°W, 5°N–5°S). Cross-equatorial transects of subsurface temperature in (g) and (h) are zonally averaged from 140° to 100°W. The bottom panel highlights the corresponding timing relative to the 17-month +TWC experiment.

anomalies due to the +TWC forcing is consistent across all ensemble members. This supports our claim that the +TWC mechanism, in isolation, is sufficient to successfully charge the tropical Pacific with warm water in boreal spring of year (1), regardless of its initial state. In addition, to further illustrate this, we calculate the probability density function (PDF) of MAM(1) WWV anomalies (Fig. 6b) for the +TWC and −TWC ensembles. The +TWC distribution of WWV values (red curve) is centered around 2.9×10^{14} m^3 with all ensemble members showing similar WWV response to the +TWC forcing. This demonstrates that +TWC wind stress forcing substantially charges the subsurface equatorial Pacific heat content and hence confirms the first hypothesized response to +TWC forcing.

3) CLIMATOLOGY FORCED INTERVAL

The aim of the climatology-forced interval of the controlled flux stage is to establish whether the +TWC induced charged equatorial Pacific is sufficient to subsequently initiate a warming in the east equatorial Pacific as an initial signal of the onset of El Niño events. The evolution of the tropical Pacific during this interval is depicted in Fig. 7, which shows the ensemble mean difference between the +TWC and NoTWC simulations. These differences reveal the subsequent evolution of the +TWC-induced anomalies in the absence of any anomalous atmospheric variability or coupled ocean–atmosphere feedbacks. Under climatological forcing, the equatorial anomalies generated by the +TWC wind stress forcing initially advect eastward along the equatorial waveguide and upward along the zonally tilted thermocline (Figs. 7c,e). By July(1), these anomalies outcrop at the surface, resulting in surface warming in the eastern equatorial Pacific (Figs. 7b,f,h). Additionally, off-equatorial positive SSH anomalies continue to propagate westward from their initial formation location (Figs. 5c,d) consistent with westward-propagating baroclinic Rossby waves, which reflect off the western boundary and may further supply equatorial Pacific heat content even though the +TWC wind stress forcing is no longer present.

This analysis shows that the eastward advection of +TWC-induced subsurface equatorial Pacific heat content anomalies results in the emergence of like-signed eastern equatorial Pacific SST anomalies. To confirm the robustness of this SST response to the TWC-related wind stress forcing, Fig. 8 displays scatterplots of the Nov(0) SST anomalies over 5°S–5°N, 135°–90°W (ENSO onset region; black box in Fig. 7b) versus Jul(1) SST in this same region for the individual ensemble members of NoTWC (black dots), +TWC (red dots), and −TWC (blue dots)

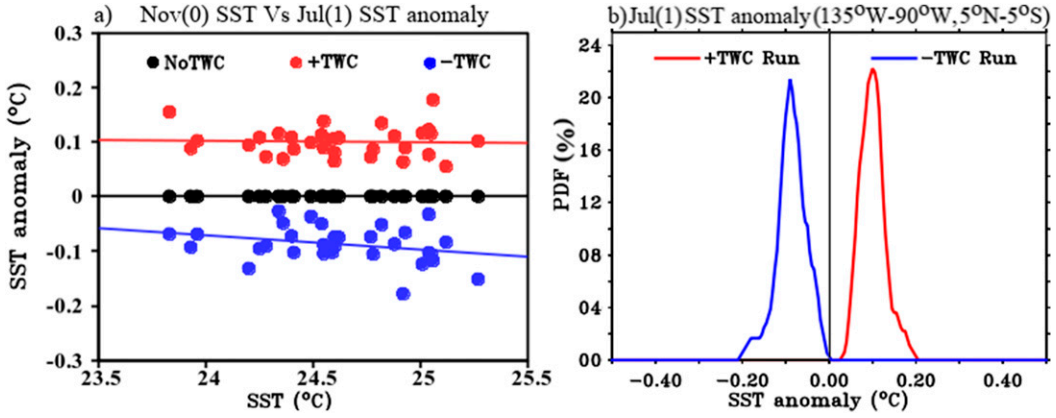

FIG. 8. (a) Scatterplot of Nov(0) SST (°C) vs Jul(1) SST anomalies for the 31 ensemble members in the ENSO onset region (average over 135°–90°W, 5°N–5°S) in Fig. 7b. For each ensemble member, Jul(1) SST anomalies are computed relative to the corresponding NoTWC SST value. Black dots correspond to the NoTWC ensembles (and by construction are identically zero), red dots correspond to the +TWC ensembles, and blue dots correspond to the −TWC ensembles. (b) PDF (%) of the Jul(1) SST anomalies in the ENSO onset region for the +TWC (red) and −TWC (blue) ensembles.

ensembles. As before, for each ensemble member, anomalies are computed with respect to the NoTWC member starting from the same initial conditions. As with the MAM(1) WWV response (Fig. 6a), the robustness of Jul(1) SST response in the onset region to the +TWC wind stress forcing is evident (red dots in Fig. 8a) and is similar across all of the ensemble members, regardless of initial SST values. To further illustrate the consistency of this surface response to TWC forcing, we calculate the PDF (Fig. 8b) of Jul(1) SST anomalies in the onset region. The +TWC ensemble experiment distribution of SST anomalies (red curve) indicates that all ensemble members show a positive SST response to the +TWC forcing. This shows that +TWC wind stress forcing does result in the emergence of significant, like-signed eastern equatorial Pacific SST anomalies (Fig. 7b), confirming the second hypothesized response to +TWC forcing.

4) FULLY COUPLED STAGE

To investigate whether the +TWC warm SST anomalies that emerge in Jul(1) develop into El Niño events, we resume thermodynamic and dynamic coupling on 1 Aug(1). We then integrate the model forward under this fully coupled configuration for the next 8 months, which allows perturbations to grow through coupled feedbacks. Figure 9 shows the subsequent growth of the equatorial Pacific anomalies. Although coupling is turned on 1 Aug(1), we choose to show Sep(1) to give the ocean anomalies enough time to interact with the overlying atmosphere. In the presence of coupling, TWC-induced SST warming over the east Pacific initiates the Bjerknes feedback by generating westerly wind anomalies (Fig. 9a) over the equatorial central Pacific (mainly west of the surface warming). Further, the off-equatorial SST anomalies can also influence these winds along the equator through the wind–evaporation–SST feedback (Amaya 2019; You and Furtado 2017). In turn, the westerly wind anomalies along the equator oppose the climatological equatorial upwelling and sustain the deepening of the thermocline in the central and eastern equatorial Pacific (Fig. 9d), further intensifying surface warming inside and beyond the boundaries of the ENSO onset region (Fig. 9a). In Oct(1), westerly wind stress anomalies become stronger over the central equatorial Pacific due to the weakening of the eastern equatorial Pacific cold tongue (2°S–2°N, 140°–100°W), driving positive SSH anomalies from 150° to 110°W and amplifying the central equatorial Pacific warming (Figs. 9b,e). Finally, in Dec(1) the +TWC ensemble exhibits an extensive surface warming pattern across the central and eastern equatorial Pacific indicative of significant but modest El Niño event with ensemble mean SST anomalies greater than +0.3°C (Fig. 9c), confirming the third hypothesized response to +TWC forcing. In addition, subsurface temperature warming during this stage amplifies as expected under the Bjerknes feedback mechanism, with continued warming along the equatorial thermocline in both the central and eastern Pacific (Figs. 9g–i).

5) THE TEMPORAL EVOLUTION OF THE EQUATORIAL PACIFIC IN THE +TWC ENSEMBLE

To depict the full evolution of the equatorial Pacific in response to +TWC wind stress forcing, Fig. 10 shows the

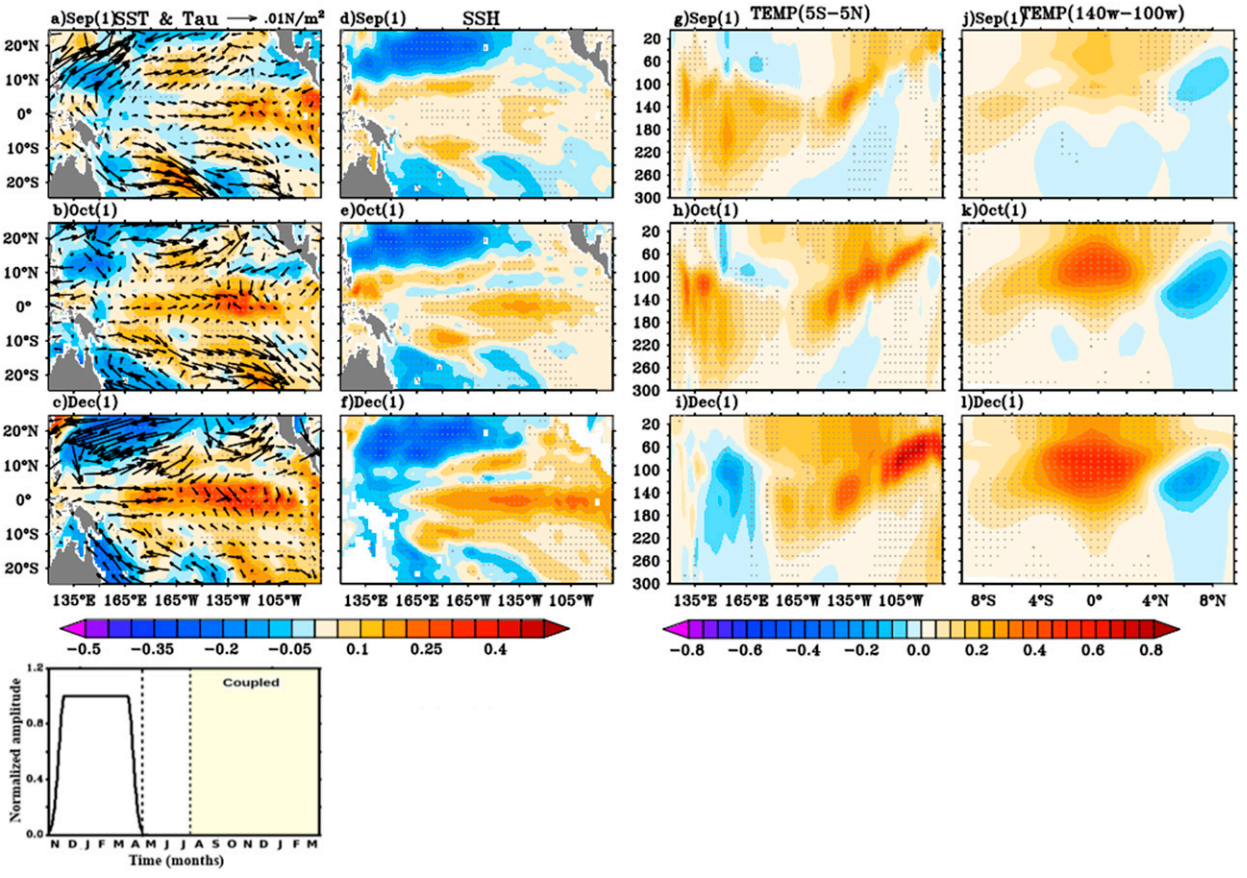

FIG. 9. As in Fig. 5, but for the +TWC ensemble mean response during the fully coupled stage in Sep(1), Oct(1), and Dec(1). Cross-equatorial transects of subsurface temperature in (j)–(l) are zonally averaged from 140° to 100°W. The bottom panel highlights the corresponding timing relative to the 17-month +TWC experiment.

time evolution of equatorial Pacific SST (Fig. 10a), SSH (Fig. 10b), and zonal wind stress (Fig. 10c) anomalies for the +TWC ensemble mean. During the +TWC anomaly forced interval, positive SSH anomalies gradually increase over the central Pacific (Fig. 10b) due to the subsurface buildup of warm water in this region, as discussed earlier. At the same time, negative zonal wind stress anomalies on the equator (Fig. 10c), a result of the prescribed +TWC wind stress pattern (Fig. 3a), generate anomalous SST cooling over the equatorial Pacific (Fig. 10a). During the climatology-forced interval [May(1)–Jul(1)], the equatorial SSH anomalies, representative of the subsurface warming, advect eastward (Fig. 10b) and result in surface warming as they outcrop in the eastern equatorial Pacific during Jun(1) and Jul(1) (Fig. 10a). During the fully coupled stage [Aug(1) onward], these warm SST anomalies (Fig. 10a) induce equatorial westerly anomalies (Fig. 10c) across the central and eastern Pacific, which in turn further deepen the thermocline (Fig. 10b) and amplify the SST warming across the central and eastern Pacific, indicative of an active Bjerknes feedback. Based on this analysis, it is evident that the emergence of +TWC-induced eastern equatorial Pacific SST anomalies does lead to the development and maturation of El Niño conditions in the Pacific.

c. −TWC ensemble results

Next, we repeat a similar analysis but with the ensemble forced with −TWC wind stress anomalies. Figure 11 depicts the tropical Pacific evolution for the ensemble mean response to −TWC wind stress forcing at various stages of the model experiment. During the anomaly forced interval, from Nov(1) through Apr(1), the ensemble mean ocean response to −TWC wind stress [Apr(1) shown in Fig. 11, top panels] is a virtual mirror image of +TWC ensemble mean response [Apr(1) shown in Fig. 5, bottom panels]. Integrated meridional transport directed away from the equator (poleward discharge of warm water) due to the −TWC wind stress curl (black contours in Fig. 11e) results in a significant cooling of subsurface temperatures along the equator (Figs. 11e,i,m). This represents the "discharged" state of the equatorial Pacific, which primes the equatorial Pacific for a La Niña

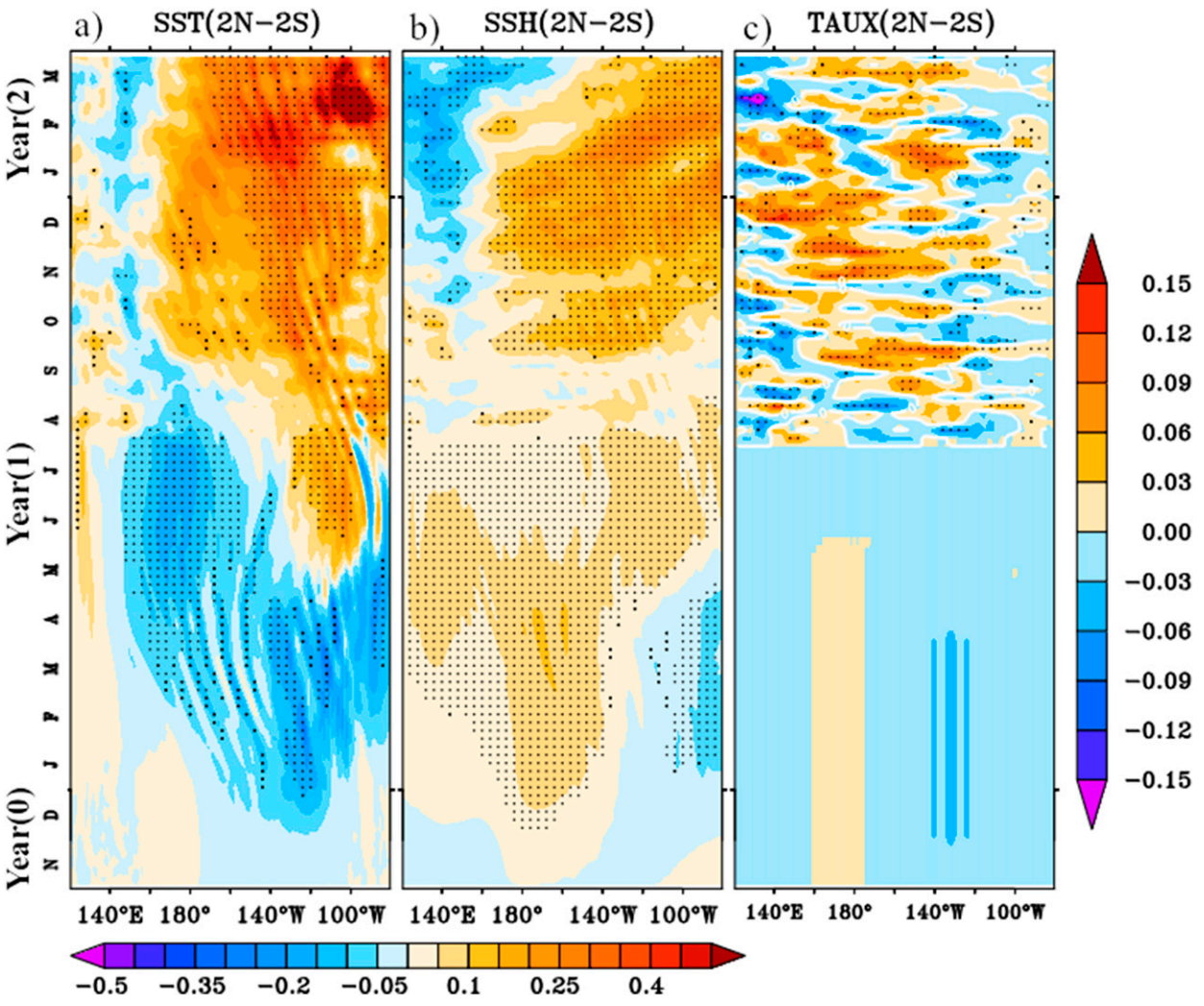

FIG. 10. Time–longitude plots of the +TWC ensemble response of (a) SST (°C), (b) SSH (m), and (c) zonal wind stress (taux; N m^{-2}) anomalies (difference between +TWC and NoTWC ensemble mean) along the equator (meridionally averaged from 2°S to 2°N) from Nov(0) to Mar(2). The white contour in (c) corresponds to 0 N m^{-2} zonal wind stress. Areas are stippled where values exceed the 90% confidence level based on a two-tailed Student's *t* test.

onset. The scatterplot of Nov(0) WWV versus the MAM(1) WWV anomaly (blue dots, Fig. 6a) and the PDF of MAM(1) WWV anomalies for the −TWC ensemble (blue line, Fig. 6b) indicate that the −TWC wind stress forces a nearly antisymmetric WWV response (approximately 2.7 × 10^{14} m^3 decrease) compared to the +TWC experiment. This response is consistent across all ensemble members. This suggests that −TWC wind stress forcing substantially discharges the equatorial Pacific heat content, which serves as an important corollary to our first hypothesized response to TWC-induced wind stress forcing.

Similar to the +TWC ensemble, during the climatology forced interval of the −TWC ensemble experiment, these negative subsurface anomalies advect toward the eastern equatorial Pacific and outcrop as negative SST anomalies in the eastern equatorial Pacific by Jul(1) (Figs. 11b,j). That said, at the end of climatology-forced stage, +TWC and −TWC forcing generates SST anomalies are not a simple mirror image (cf. Figs. 7b,j and 11b,f). Instead, a small asymmetry develops in the far eastern equatorial Pacific SSTs between the two experiments. The cold SST anomaly that emerges in the −TWC experiments is located slightly west of its +TWC counterpart, due to slower equatorward and eastward advection of subsurface cold anomalies in −TWC simulation (not shown). Thus, the pre-existing warm SST anomalies in the far eastern equatorial Pacific (eastern edge of box in Fig. 11b) do not fully dissipate, resulting in an east–west SST gradient in the −TWC experiment. These differences in the eastern equatorial SST anomalies in the onset region are more apparent in the scatterplot and PDF for the −TWC

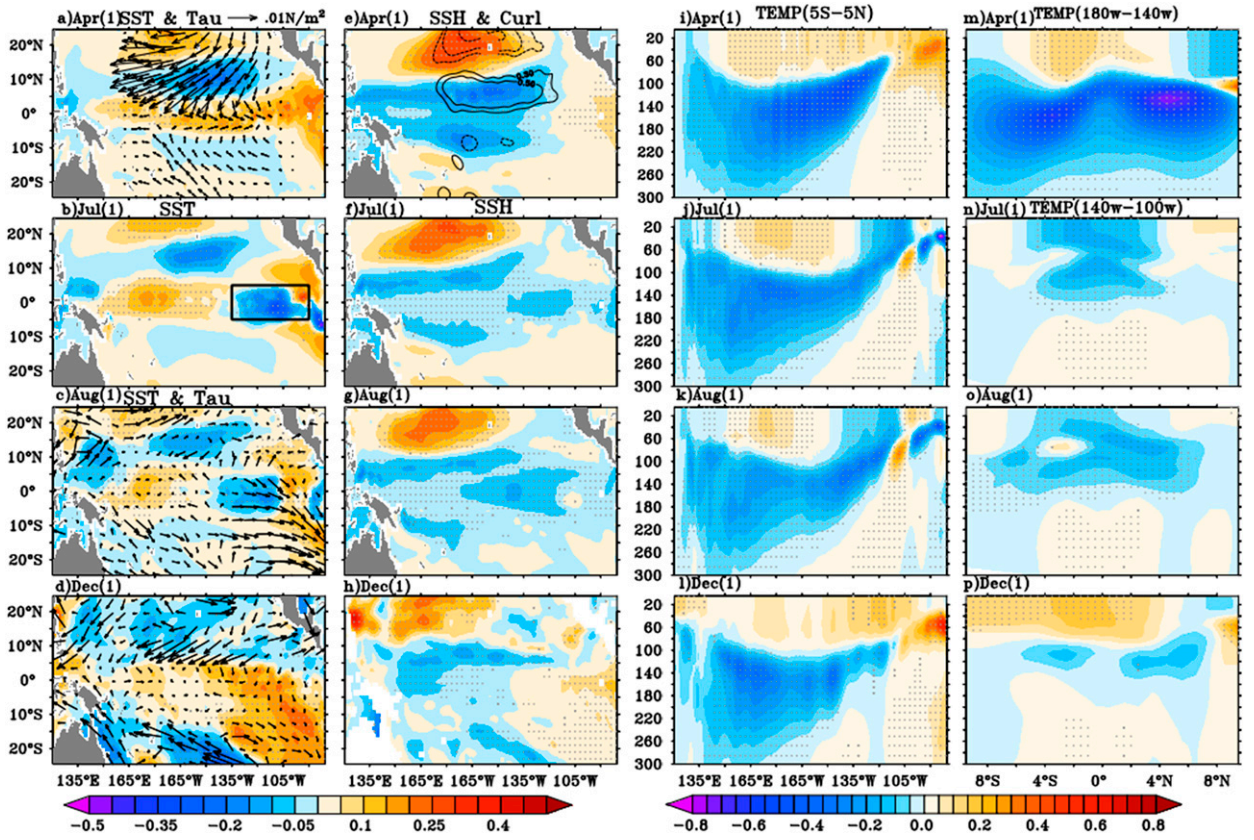

FIG. 11. Ensemble mean model response to −TWC wind stress forcing during the anomaly-forced interval of the controlled flux stage in Apr(1), the climatology-forced interval of the controlled flux stage in Jul(1), and the fully coupled stage in Aug(1) and Dec(1). The difference between −TWC and NoTWC ensemble mean for (a)–(d) SST (°C; shaded) and wind stress (tau; N m^{-2}; vectors), (e)–(h) SSH (m; shaded) and wind stress curl (10^{-8} N m^{-3}; contours with values ±0.3, ±0.5, and ±1), (i)–(l) meridionally averaged (5°N–5°S) subsurface temperature, and (m)–(p) zonally averaged [180°–140°W for (m) and 140° to 100°W for (n)–(p)] subsurface temperature. Stippling shows regions where ensemble mean differences are significant with a 90% confidence level based on a two-tailed Student's *t* test.

ensembles in Fig. 8. Despite this slight asymmetry, anomalous cooling of the eastern equatorial Pacific is still found across all ensemble members at this stage of the experiment (blue curve in Fig. 8b). Hence, we additionally argue that −TWC wind stress forcing results in the emergence of significant, like-signed eastern equatorial Pacific SST anomalies, which is a corollary to the second hypothesized response to TWC-induced wind stress forcing.

As soon as the coupling is engaged, however, a marked asymmetry arises between the +TWC and −TWC experiments. Instead of finding the expected easterly anomalies over the central equatorial Pacific (as a negative analog of the +TWC experiments), in the −TWC experiments, the east–west SST gradient in the eastern equatorial Pacific induces local westerly anomalies in Aug(1) (Fig. 11c). A subsequent mixed layer heat-budget analysis (not shown) indicates that during the beginning of the fully coupled stage for the −TWC experiments, the net heat flux associated with the westerly wind anomalies results in a temperature tendency that suppresses the growth of the La Niña conditions in the onset region (Figs. 11k,l). As the surface waters warm, they, along with the westerly wind stress anomalies, expand westward over the central equatorial Pacific, resulting in weak El Niño–like conditions (Fig. 11d).

4. Evolution of individual +TWC and −TWC ensemble members

To determine the robustness (or lack thereof) of the imposed +TWC/−TWC wind stress anomaly forcing on the development of like-signed ENSO events, we analyze the evolution of the individual ensemble members across the full experimental integration. Figure 12 shows the time evolution of Niño-3.4 SST and equatorial Pacific WWV anomalies (both calculated with respect to their corresponding NoTWC branch simulation) for the individual ensemble members from the +TWC (red) and −TWC (blue) experiments. The broomstick-like curves exhibit close clustering of all ensemble members around their

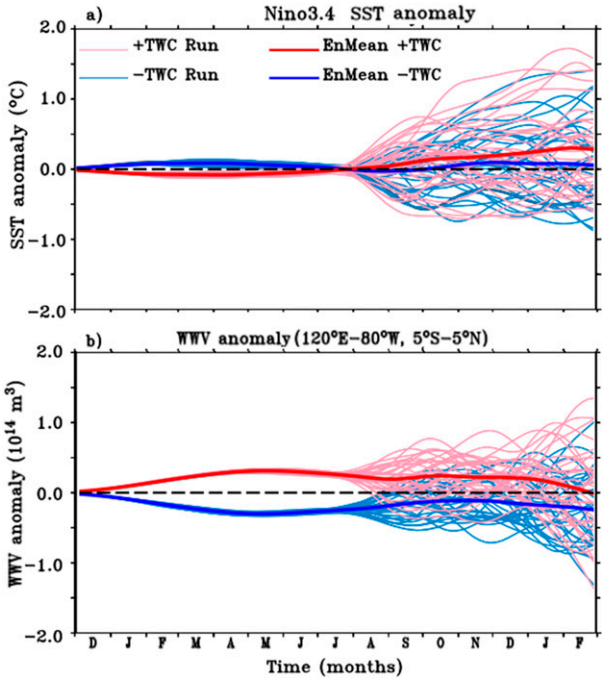

FIG. 12. The 5-day mean (a) Niño-3.4 SST (°C) anomalies with 3-month smoothing for the 31 +TWC (thin red lines) and −TWC (thin blue lines) ensembles computed by removing the corresponding NoTWC ensemble member. Thick red and blue lines correspond to the +TWC and −TWC ensemble means, respectively. The black dashed line shows the 0°C Niño-3.4 SST anomaly. (b) As in (a), but for WWV anomalies (10^{14} m^3) averaged over 120°E–80°W, 5°N–5°S.

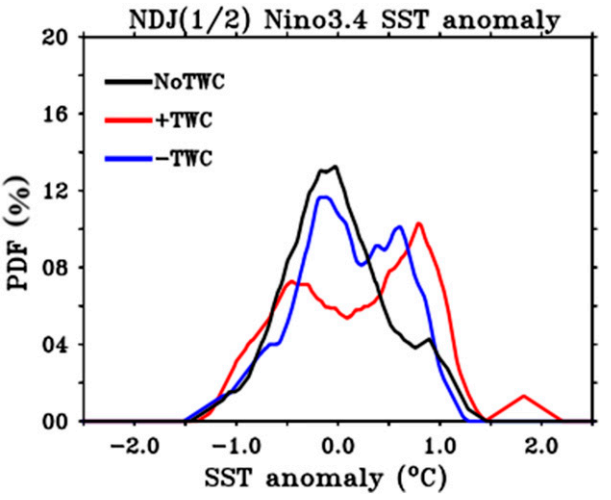

FIG. 13. Probability density function of the NDJ(1/2) SST (°C) anomalies in the Niño-3.4 region calculated with respect to the NoTWC ensemble mean for the NoTWC (black), +TWC (red), and −TWC (blue) ensembles.

ensemble means during the controlled flux stage from Nov(0) to Jul(1), as expected. During this stage, although the SST response in the Niño-3.4 region is weak, the narrow distribution of the WWV anomalies (Fig. 12b) confirms that the +TWC/−TWC forcing consistently provides sufficient fuel (subsurface preconditioning of equatorial Pacific heat content) in boreal summer for a like-signed ENSO event to develop in the subsequent winter.

However, once the coupling is turned on in Aug(1), the individual ensemble members in either experiment quickly diverge, evidenced by widening of the plumes in both the Niño-3.4 SST and WWV anomalies. Despite the large ensemble spread, the positive Niño-3.4 values of the +TWC ensemble mean indicate the presence of modest El Niño–like warming (thick red line in Fig. 12a), whereas the −TWC forcing is unable to consistently develop La Niña–like cooling (blue lines in Fig. 12a) as discussed in the previous sections. These results demonstrate that in our model, the response of Niño-3.4 SST is not linearly dependent on the sign of the anomalous TWC forcing applied once coupling resumes.

To further illustrate the Niño-3.4 SST response to TWC forcing, we calculate the PDF of the NDJ(1/2) Niño-3.4 SST anomalies (Fig. 13) for the NoTWC, +TWC, and −TWC ensembles. Since the NoTWC integrations only contain internal variability resulting from the influence of coupling, here we calculate SST anomalies relative to the NoTWC ensemble mean (rather than relative to the corresponding the NoTWC ensemble members). While the difference in the means of the +TWC and NoTWC distributions is small (less than 0.2°C), the +TWC distribution (red line) is positively skewed, bimodal, and significantly different from the corresponding NoTWC distribution (black line) at the 90% confidence level. Importantly, the probability of an El Niño is substantially larger in the +TWC than the NoTWC experiment. Specifically,14 out of 31 (45%) of the +TWC ensemble members exceed 0.5°C warming in the Niño-3.4 region in boreal winter, which is nearly 3 times as often as in the NoTWC experiment (5 out of 31 members). In addition, an analysis of the location of the center of heat index (CHI) indicates that within the +TWC ensemble, ~80% of the warm members lie to the east of 150°W, the longitude separating the Niño-4 (i.e., central Pacific) region from the Niño-3 (i.e., eastern Pacific) region, suggesting that +TWC forcing has a tendency to produce eastern Pacific El Niño events (by comparison, the NoTWC experiment shows no preference for one type of ENSO event over the other). In contrast the −TWC PDF (blue line) is not significantly different from the NoTWC distribution although, as with the +TWC experiment, the bimodal distribution is skewed positive rather than skewed negative with more substantial warming events (9 members) than in the NoTWC experiment, again indicating a nonlinear

response of the ENSO system to the sign of the TWC-related wind stress forcing.

5. Summary

In this study, TWC favorable (+TWC) or unfavorable (−TWC) wind stress forcing is imposed in a set of CESM1 coupled model experiments to examine the ENSO response to the TWC mechanism. For both +TWC and −TWC scenarios, we integrate an ensemble experiment, in addition to a control ensemble experiment (NoTWC), in which no TWC forcing is applied. Each ensemble member is branched from an ENSO-neutral initial condition. Initially, each member is integrated with the ocean component essentially decoupled from the atmosphere, with the ocean forced by climatological thermal fluxes and prescribed wind stress anomalies associated with +TWC, −TWC, or NoTWC (anomalies = 0) superimposed upon the climatological wind stress. For each +TWC and −TWC ensemble member, anomalous forcing is imposed through the first winter, Nov(0) to Apr(1), and then the model evolves under purely climatological forcing until the end of Jul(1). This "controlled flux stage" of the experiment allows 1) the +TWC (−TWC) mechanism to "charge" ("discharge") the warm water volume in the equatorial Pacific; 2) the associated subsurface warming/cooling to advect eastward along the equatorial thermocline; and 3) the outcropping of the subsurface anomalies to induce initial warm/cold SST anomalies in the eastern equatorial Pacific (ENSO onset region). Next, to allow these TWC-forced SST anomalies to grow via coupled feedbacks, each ensemble member is integrated in a "fully coupled stage" for the remainder of the experiment, from Aug(1) to the following winter, Mar(2). The NoTWC experiment is similar except that the ensemble members are integrated under climatological forcing during the entire controlled flux stage from Nov(0) to Jul(1).

We find a robust subsurface ocean response to +TWC and −TWC forcing relative to the NoTWC experiment across the equatorial Pacific. Wintertime +TWC forcing generates a buildup of subsurface heat content through equatorward mass transport and leads to a charged state in the equatorial Pacific with large warm (positive) subsurface temperature anomalies along the thermocline during the following spring (Fig. 5), consistent with Anderson et al. (2013). Similarly, wintertime −TWC forcing drives meridional mass transport away from the equator, discharges the equatorial Pacific heat content poleward and results in cool (negative) equatorial Pacific subsurface temperature anomalies (Fig. 11, top panels). For both +TWC and −TWC experiments, these subsurface temperature anomalies then advect eastward and upward along the equatorial thermocline from May(1) to Jul(1) and consistently produce warm (+TWC) or cool (−TWC) eastern equatorial Pacific SST anomalies in Jul(1) (Figs. 7b and 11b, respectively), consistent with the onset of like-signed ENSO events. Thus, the system is primed with favorable conditions upon which the Bjerknes feedback can act and potentially develop like-signed ENSO events the following winter. These responses to TWC forcing are consistent across all ensemble members (Figs. 6 and 8). Overall, the +TWC/−TWC forcing consistently "primes" the equatorial Pacific for like-signed ENSO event development.

Notably, even though the oceanic response to TWC forcing is fairly symmetric in the +TWC and −TWC experiments, once the coupling is engaged we find an asymmetry in the subsequent ENSO development. The +TWC-induced eastern equatorial Pacific warming generates westerly wind stress anomalies over the central equatorial Pacific and on average leads to an El Niño–like warming in the following winter [NDJ(1/2)], as hypothesized in Anderson and Perez (2015). In contrast, the −TWC-induced eastern equatorial Pacific cooling along with pre-existing warming in the far eastern equatorial Pacific generates an east–west SST gradient. This SST gradient triggers westerly wind stress anomalies over the eastern equatorial Pacific. These localized westerly wind anomalies inhibit the emergence of the cold subsurface temperature anomalies, resulting in a reversal of the SST anomalies and the subsequent development of weak warming in the eastern equatorial and southeast Pacific.

One question that arises is why, given the robust and consistent charging (discharging) of equatorial subsurface heat content and the subsequent initial east Pacific warm (cold) SST anomalies in the +TWC (−TWC) experiments, do these experiments fail to consistently result in the development of El Niño (La Niña) events once the ocean and atmosphere are fully coupled? In addition to the coupled feedbacks mentioned above, many studies have shown that stochastic atmospheric variability (e.g., wind bursts) plays a critical role in the evolution of ENSO events (Fedorov et al. 2015; Levine and McPhaden 2016; Hu and Fedorov 2016, 2017; Larson and Kirtman 2017; Puy et al. 2017; Izumo et al. 2018). Therefore, we hypothesize that stochastic variability is responsible for the inconsistent (large spread) ENSO response in the TWC experiments. Indeed, Larson and Kirtman (2017) estimate that ocean preconditioning associated with the traditional Jin (1997) recharge/discharge explains just 30% of ENSO variability in a coupled model experiment similar to this one, whereas roughly 70% can be explained by stochastic variability alone. It is also possible that the nearly but not quite neutral initial conditions may have played a role in the large ensemble spread and

bimodal distribution of the ENSO response. Analysis of the interaction between stochastic forcing, initial conditions, and the TWC mechanism is beyond the scope of this paper, but will be the subject of future study.

It is also important to note that our experiments only consider the dynamic response of the tropical Pacific to NPO-induced changes in extratropical winds, and do not include the corresponding thermodynamically coupled air–sea interactions associated with the SFM and NPMM mechanisms. The relative contribution of the TWC mechanism (dynamic interactions) and NPMM mechanism (thermodynamic interactions) on the development of subsequent ENSO events, along with their combined effect, might produce a more pronounced ENSO response and will also be explored in future studies.

Acknowledgments. This work was supported by NSF Grants AGS-1547137 (SC, RCP), AGS-1547412 (BTA, VP), and AGS-1547398 (BSG). SC and RCP acknowledge the NOAA/Atlantic Oceanographic and Meteorological Laboratory. SC was supported under the auspices of the Cooperative Institute for Marine and Atmospheric Studies (CIMAS), a cooperative institute of the University of Miami and NOAA, cooperative agreement NA10OAR4320143. We would like to acknowledge high-performance computing support from Cheyenne (https://doi.org/10.5065/D6RX99HX) provided by NCAR's Computational and Information Systems Laboratory, sponsored by the National Science Foundation. We also thank the three anonymous reviewers and Sang-Ki Lee for their helpful comments and suggestions.

APPENDIX

Generation of TWC Wind Stress Fields

To identify TWC-related wind stress fields from within the SODAsi.3 reanalysis product we seek to isolate the boreal winter tropical wind stress field $\tau_{x'}$ that 1) has the highest correlation with tropical SST variability during the following boreal winter and 2) is independent of the concurrent ENSO state. To do so, we use monthly SST and zonal wind stress τ_x from the SODAsi.3 and 20CRv2c datasets, respectively. Since the +TWC-related wind stress anomalies comprise both westerly anomalies (i.e., weakened trade winds) in the central North Pacific and weak easterly anomalies (i.e., strengthened trade winds) in the eastern equatorial Pacific, following the method of Anderson and Perez (2015; cf. their Fig. 14a), we isolate the central and eastern Pacific wind stress anomalies by restricting the reconstructed fields to the region between 180° and 120°W, and from 20°S to 20°N, using a 20° wide Gaussian taper (Anderson and Perez 2015; cf. their Fig. 14a) as shown in Fig. 3a. This procedure removes possible impacts from concurrent western equatorial Pacific wind stress fields, but retains equatorial wind stress fields over the central and eastern Pacific that can generate an off-equatorial wind stress curl and vertically integrated mass transport upon which the TWC mechanism relies. Furthermore, because both ENSO and TWC are most active during boreal winter, the variables are seasonally averaged from November to January for SST (Trenberth 1997) and from November to February for τ_x and the seasonal means are linearly detrended across all years (Anderson and Perez 2015).

To further improve robustness of the results, the data processing described above is run identically on all eight ensemble members available from the two reanalysis products (as opposed to their ensemble means, which is a more conventional value to analyze). These eight anomaly fields are then concatenated along the time dimension, resulting in time series spanning $8 \times 60 = 480$ years. This strategy assures that interesting internal variability from each ensemble member is retained, while still using all realizations to constrain the results and reduce their sensitivity to the noise that a single member could be carrying. As a sensitivity test, the analysis was repeated twice: 1) on each ensemble member separately whose results were then averaged, and 2) on the ensemble mean. The results (not shown) were highly similar and the time-concatenated approach was chosen for our study.

Having obtained the spatiotemporal evolution of boreal winter, tropical Pacific wind stress, and SST variations, we next sought to identify precursor modes of wind stress variability that precede large-scale changes in the boreal winter SST structure the following year by adopting a variant of the canonical correlation analysis (CCA) used by Anderson (2003). As in previous analyses (e.g., Bretherton et al. 1992; Graham et al. 1987) we first isolate large-scale modes of variability in both fields through EOF analysis and then, following the method outlined by Anderson (2003), apply CCA to the leading EOF time series of boreal winter, tropical Pacific zonal wind stress, and the following boreal winter's tropical Pacific SST. The subset includes the first 10 modes for SST and the first 9 modes for the wind stress fields. To avoid concurrent, ENSO-related wind stress anomalies from biasing the TWC-related wind stress reconstructions, we followed the approach documented by Larson and Kirtman (2013) and remove these anomalies by excluding the first EOF of τ_x—which captures the time evolution of ENSO-related wind stress anomalies—from the CCA. As a robustness test, ENSO-related wind stress anomalies are also linearly removed using the

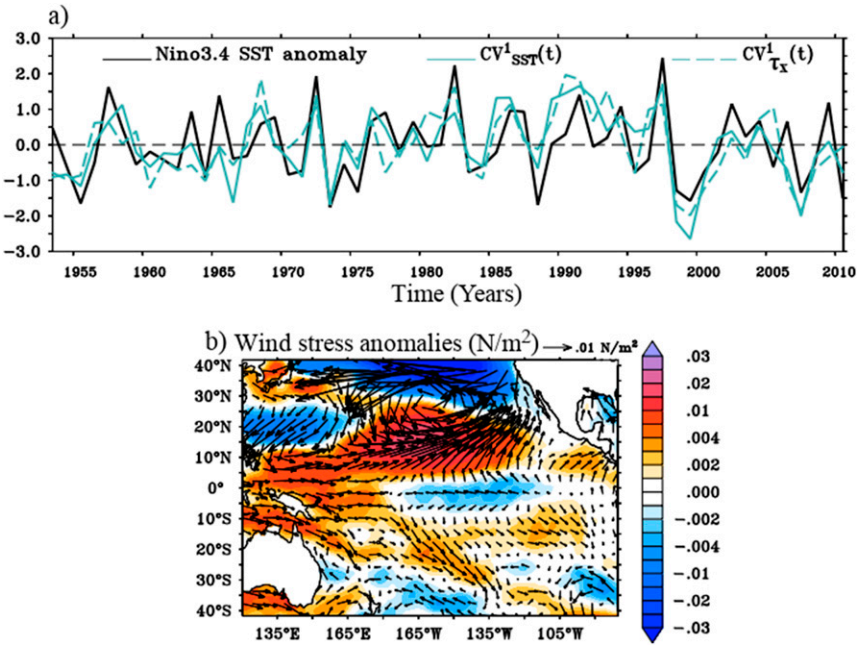

FIG. A1. (a) Canonical variables of SST [$CV^1_{SST}(t)$; thick green line] and zonal winds [$CV^1_{\tau_x}(t)$; dotted green line] for the first canonical factor relating boreal winter (November–February) tropical Pacific wind stress variations to SST variations the following winter (November–January). Also shown is the November–January Niño-3.4 index (black line) concurrent with $CV^1_{SST}(t)$. The $CV^1_{\tau_x}(t)$ time series are plotted with respect to January of a given year while the $CV^1_{SST}(t)$ and Niño-3.4 time series are the values for the following winter. (b) Weighted mean zonal wind stress (N m^{-2}; shaded) and total wind stress (N m^{-2}; vectors) anomalies associated with positive values of $CV^1_{\tau_x}(t)$, representative of +TWC conditions.

concurrent Niño-3.4 index and the final results are identical (not shown).

The CCA analysis returns paired time series, one for SST and the other for τ_x, and they are sorted such that the first mode is the one with the highest correlation between paired time series (Fig. 3a). Using the first canonical variable for τ_x, $CV^1_{\tau_x}(t)$, the wind fields of TWC were reconstructed using a weighted composite algorithm. The weights are defined by $W^1_{\tau_x}(t)$, where

$$W^1_{\tau_x}(t) = \begin{cases} CV^1_{\tau_x}(t), & \text{if } CV^1_{\tau_x}(t) > 0, \\ 0, & \text{otherwise.} \end{cases}$$

Given the anomaly fields of zonal and meridional winds at grid space s and time t, $\tau_x(s,t)$ and $\tau_y(s,t)$, respectively, the reconstructed fields are equal to

$$\tilde{\tau}_x(s) = \frac{\sum_t \tau_x(s,t) \times W^1_{\tau_x}(t)}{\sum_t W^1_{\tau_x}(t)},$$

$$\text{and } \tilde{\tau}_y(s) = \frac{\sum_t \tau_y(s,t) \times W^1_{\tau_x}(t)}{\sum_t W^1_{\tau_x}(t)}.$$

Figure A1a shows the time evolution of the first canonical variable for SST and τ_x, along with the Niño-3.4 time series. Figure A1b shows the reconstructed wind stress pattern associated with the +TWC over the tropical Pacific.

REFERENCES

Alexander, M. A., 1992: Midlatitude atmosphere–ocean interaction during El Niño. Part I: The North Pacific Ocean. *J. Climate*, **5**, 944–958, https://doi.org/10.1175/1520-0442(1992)005<0944:MAIDEN>2.0.CO;2.

——, D. J. Vimont, P. Chang, and J. D. Scott, 2010: The impact of extratropical atmospheric variability on ENSO: Testing the seasonal footprinting mechanism using coupled model experiments. *J. Climate*, **23**, 2885–2901, https://doi.org/10.1175/2010JCLI3205.1.

Amaya, D. J., 2019: The Pacific meridional mode and ENSO: A review. *Curr. Climate Change Rep.*, **5**, 296–307, https://doi.org/10.1007/s40641-019-00142-x.

Anderson, B. T., 2003: Tropical Pacific sea-surface temperatures and preceding sea-level pressure anomalies in the subtropical North Pacific. *J. Geophys. Res.*, **108**, 4732, https://doi.org/10.1029/2003JD003805.

——, 2004: Investigation of a large-scale mode of ocean-atmosphere variability and its relation to tropical Pacific sea surface temperature anomalies. *J. Climate*, **17**, 4089–4098,

https://doi.org/10.1175/1520-0442(2004)017<4089:IOALMO>2.0.CO;2.

——, 2007: Intraseasonal atmospheric variability in the extratropics and its relation to the onset of tropical Pacific sea surface temperature anomalies. *J. Climate*, **20**, 926–936, https://doi.org/10.1175/JCLI4036.1.

——, and E. Maloney, 2006: Interannual tropical Pacific sea surface temperatures and their relation to preceding sea level pressures in the NCAR CCSM2. *J. Climate*, **19**, 998–1012, https://doi.org/10.1175/JCLI3674.1.

——, and R. C. Perez, 2015: ENSO and non-ENSO induced charging and discharging of the equatorial Pacific. *Climate Dyn.*, **45**, 2309–2327, https://doi.org/10.1007/s00382-015-2472-x.

——, E. Maloney, R. Perez, and A. Karspeck, 2013: Triggering of El Niño onset through the trade wind induced charging of the equatorial Pacific. *Geophys. Res. Lett.*, **40**, 1212–1216, https://doi.org/10.1002/grl.50200.

——, P. Hassanzadeh, and R. Caballero, 2017: Persistent anomalies of the extratropical Northern Hemisphere wintertime circulation as an initiator of El Niño/Southern Oscillation events. *Sci. Rep.*, **7**, 10145, https://doi.org/10.1038/s41598-017-09580-9.

Barnston, A. G., M. K. Tippett, M. L. L'Heureux, S. Li, and D. G. DeWitt, 2012: Skill of real-time seasonal ENSO model predictions during 2002–11: Is our capability increasing? *Bull. Amer. Meteor. Soc.*, **93**, 631–651, https://doi.org/10.1175/BAMS-D-11-00111.1.

Bjerknes, J., 1969: Atmospheric teleconnections from the equatorial Pacific. *Mon. Wea. Rev.*, **97**, 163–172, https://doi.org/10.1175/1520-0493(1969)097<0163:ATFTEP>2.3.CO;2.

Bretherton, C. S., C. Smith, and J. M. Wallace, 1992: An intercomparison of methods for finding coupled patterns in climate data. *J. Climate*, **5**, 541–560, https://doi.org/10.1175/1520-0442(1992)005<0541:AIOMFF>2.0.CO;2.

Carton, J. A., and B. S. Giese, 2008: A reanalysis of ocean climate using Simple Ocean Data Assimilation (SODA). *Mon. Wea. Rev.*, **136**, 2999–3017, https://doi.org/10.1175/2007MWR1978.1.

Chakravorty, S., J. S. Chowdary, and C. Gnanaseelan, 2013: Spring asymmetric mode in the tropical Indian Ocean: Role of El Niño and IOD. *Climate Dyn.*, **40**, 1467–1481, https://doi.org/10.1007/s00382-012-1340-1.

——, C. Gnanaseelan, and P. A. Pillai, 2016: Combined influence of remote and local SST forcing on Indian summer monsoon rainfall variability. *Climate Dyn.*, **47**, 2817–2831, https://doi.org/10.1007/s00382-016-2999-5.

Chang, P., L. Zhang, R. Saravanan, D. J. Vimont, J. C. H. Chiang, L. Ji, H. Seidel, and M. K. Tippett, 2007: Pacific meridional mode and El Niño–Southern Oscillation. *Geophys. Res. Lett.*, **34**, L16608, https://doi.org/10.1029/2007GL030302.

Chen, Z., B. Gan, L. Wu, and F. Jia, 2018: Pacific–North American teleconnection and North Pacific Oscillation: Historical simulation and future projection in CMIP5 models. *Climate Dyn.*, **50**, 4379–4403, https://doi.org/10.1007/s00382-017-3881-9.

Chiang, J. C. H., and D. J. Vimont, 2004: Analogous Pacific and Atlantic meridional modes of tropical atmosphere–ocean variability. *J. Climate*, **17**, 4143–4158, https://doi.org/10.1175/JCLI4953.1.

Clarke, A. J., S. V. Gorder, and G. Colantuono, 2007: Wind stress curl and ENSO discharge/recharge in the equatorial Pacific. *J. Phys. Oceanogr.*, **37**, 1077–1091, https://doi.org/10.1175/JPO3035.1.

Danabasoglu, G., S. C. Bates, B. P. Briegleb, S. R. Jayne, M. Jochum, W. G. Large, S. Peacock, and S. G. Yeager, 2012: The CCSM4 ocean component. *J. Climate*, **25**, 1361–1389, https://doi.org/10.1175/JCLI-D-11-00091.1.

DiNezio, P. N., C. Deser, Y. Okumura, and A. Karspeck, 2017: Predictability of 2-year La Niña events in a coupled general circulation model. *Climate Dyn.*, **49**, 4237–4261, https://doi.org/10.1007/s00382-017-3575-3.

Fedorov, A. V., S. Hu, M. Lengaigne, and E. Guilyardi, 2015: The impact of westerly wind bursts and ocean initial state on the development, and diversity of El Niño events. *Climate Dyn.*, **44**, 1381–1401, https://doi.org/10.1007/s00382-014-2126-4.

Gettelman, A., and Coauthors, 2010: Global simulations of ice nucleation and ice supersaturation with an improved cloud scheme in the Community Atmosphere Model. *J. Geophys. Res.*, **115**, D18216, https://doi.org/10.1029/2009JD013797.

Giese, B. S., and S. Ray, 2011: El Niño variability in Simple Ocean Data Assimilation (SODA), 1871–2008. *J. Geophys. Res.*, **116**, C02024, https://doi.org/10.1029/2010JC006695.

——, H. F. Seidel, G. P. Compo, and P. D. Sardeshmukh, 2016: An ensemble of ocean reanalyses for 1815–2013 with sparse observational input. *J. Geophys. Res. Oceans*, **121**, 6891–6910, https://doi.org/10.1002/2016JC012079.

Graham, N. E., J. Michaelsen, and T. P. Barnett, 1987: An investigation of the El Niño–Southern Oscillation cycle with statistical models: 1. Predictor field characteristics. *J. Geophys. Res.*, **92**, 14 251–14 270, https://doi.org/10.1029/JC092iC13p14251.

Guilyardi, E., P. Braconnot, F.-F. Jin, S. T. Kim, M. Kolasinski, T. Li, and I. Musat, 2009: Atmosphere feedbacks during ENSO in a coupled GCM with a modified atmospheric convection scheme. *J. Climate*, **22**, 5698–5718, https://doi.org/10.1175/2009JCLI2815.1.

Hu, S., and A. V. Fedorov, 2016: Exceptionally strong easterly wind burst stalling El Niño of 2014. *Proc. Natl. Acad. Sci. USA*, **113**, 2005–2010, https://doi.org/10.1073/pnas.1514182113.

——, and ——, 2017: The extreme El Niño of 2015–2016: The role of westerly and easterly wind bursts, and preconditioning by the failed 2014 event. *Climate Dyn.*, **52**, 7339–7357, https://doi.org/10.1007/s00382-017-3531-2.

Hurrell, J. W., and Coauthors, 2013: The Community Earth System Model: A framework for collaborative research. *Bull. Amer. Meteor. Soc.*, **94**, 1339–1360, https://doi.org/10.1175/BAMS-D-12-00121.1.

Izumo, T., M. Lengaigne, J. Vialard, I. Suresh, and Y. Planton, 2018: On the physical interpretation of the lead relation between warm water volume and the El Niño Southern Oscillation. *Climate Dyn.*, **52**, 2923–2942, https://doi.org/10.1007/s00382-018-4313-1.

Jin, F.-F., 1997: An equatorial ocean recharge paradigm for ENSO. Part I: Conceptual model. *J. Atmos. Sci.*, **54**, 811–829, https://doi.org/10.1175/1520-0469(1997)054<0811:AEORPF>2.0.CO;2.

Large, W. G., and S. G. Yeager, 2009: The global climatology of an interannually varying air–sea flux data set. *Climate Dyn.*, **33**, 341–364, https://doi.org/10.1007/s00382-008-0441-3.

Larson, S., and B. Kirtman, 2013: The Pacific meridional mode as a trigger for ENSO in a high-resolution coupled model. *Geophys. Res. Lett.*, **40**, 3189–3194, https://doi.org/10.1002/grl.50571.

——, and ——, 2014: The Pacific meridional mode as an ENSO precursor and predictor in the North American multimodel ensemble. *J. Climate*, **27**, 7018–7032, https://doi.org/10.1175/JCLI-D-14-00055.1.

——, and B. P. Kirtman, 2015: Revisiting ENSO coupled instability theory and SST error growth in a fully coupled model. *J. Climate*, **28**, 4724–4742, https://doi.org/10.1175/JCLI-D-14-00731.1.

——, and ——, 2017: Drivers of coupled model ENSO error dynamics and the spring predictability barrier. *Climate Dyn.*, **48**, 3631–3644, https://doi.org/10.1007/s00382-016-3290-5.

——, and ——, 2019: Linking preconditioning to extreme ENSO events and reduced ensemble spread. *Climate Dyn.*, **52**, 7417–7433, https://doi.org/10.1007/s00382-017-3791-x.

——, K. V. Pegion, and B. P. Kirtman, 2018a: The South Pacific meridional mode as a thermally driven source of ENSO amplitude modulation and uncertainty. *J. Climate*, **31**, 5127–5145, https://doi.org/10.1175/JCLI-D-17-0722.1.

——, D. J. Vimont, A. C. Clement, and B. P. Kirtman, 2018b: How momentum coupling affects SST variance and large-scale Pacific climate variability in CESM. *J. Climate*, **31**, 2927–2944, https://doi.org/10.1175/JCLI-D-17-0645.1.

Lau, N.-C., and M. J. Nath, 1996: The role of the atmospheric bridge in linking tropical Pacific ENSO events to extratropical SST anomalies. *J. Climate*, **9**, 2036–2057, https://doi.org/10.1175/1520-0442(1996)009<2036:TROTBI>2.0.CO;2.

Levine, A. F. Z., and M. J. McPhaden, 2016: How the July 2014 easterly wind burst gave the 2015–2016 El Niño a head start. *Geophys. Res. Lett.*, **43**, 6503–6510, https://doi.org/10.1002/2016GL069204.

Li, T., 1997: Phase transition of the El Niño–Southern Oscillation: A stationary SST mode. *J. Atmos. Sci.*, **54**, 2872–2887, https://doi.org/10.1175/1520-0469(1997)054<2872:PTOTEN>2.0.CO;2.

Linkin, M. E., and S. Nigam, 2008: The North Pacific Oscillation–west Pacific teleconnection pattern: Mature-phase structure and winter impacts. *J. Climate*, **21**, 1979–1997, https://doi.org/10.1175/2007JCLI2048.1.

Liu, Z., and S. Xie, 1994: Equatorward propagation of coupled air–sea disturbances with application to the annual cycle of the eastern tropical Pacific. *J. Atmos. Sci.*, **51**, 3807–3822, https://doi.org/10.1175/1520-0469(1994)051<3807:EPOCAD>2.0.CO;2.

McPhaden, M. J., and Coauthors, 1998: The Tropical Ocean–Global Atmosphere observing system: A decade of progress. *J. Geophys. Res.*, **103**, 14 169–14 240, https://doi.org/10.1029/97JC02906.

——, S. E. Zebiak, and M. H. Glantz, 2006: ENSO as an integrating concept in Earth science. *Science*, **314**, 1740–1745, https://doi.org/10.1126/science.1132588.

Meinen, C. S., and M. J. McPhaden, 2000: Observations of warm water volume changes in the equatorial Pacific and their relationship to El Niño and La Niña. *J. Climate*, **13**, 3551–3559, https://doi.org/10.1175/1520-0442(2000)013<3551:OOWWVC>2.0.CO;2.

Min, Q., J. Su, R. Zhang, and X. Rong, 2015: What hindered the El Niño pattern in 2014? *Geophys. Res. Lett.*, **42**, 6762–6770, https://doi.org/10.1002/2015GL064899.

Neale, R. B., and Coauthors, 2012: Description of the NCAR Community Atmosphere Model (CAM 5.0). NCAR Tech. Note NCAR/TN-486+STR, 274 pp., www.cesm.ucar.edu/models/cesm1.0/cam/docs/description/cam5_desc.pdf.

Philander, S. G., 1983: El Niño Southern Oscillation phenomena. *Nature*, **302**, 295–301, https://doi.org/10.1038/302295a0.

——, 1990: *El Niño and La Niña, and the Southern Oscillation*. Academic Press, 289 pp.

Pierce, D., T. Barnett, and M. Latif, 2000: Connections between the Pacific Ocean tropics and midlatitudes on decadal timescales. *J. Climate*, **13**, 1173–1194, https://doi.org/10.1175/1520-0442(2000)013%3C1173:CBTPOT%3E2.0.CO;2.

Puy, M., and Coauthors, 2017: Influence of westerly wind events stochasticity on El Niño amplitude: The case of 2014 vs. 2015. *Climate Dyn.*, **52**, 7435–7454, https://doi.org/10.1007/s00382-017-3938-9.

Rasmusson, E. M., and T. H. Carpenter, 1982: Variations in tropical sea surface temperature and surface wind fields associated with the Southern Oscillation/El Niño. *Mon. Wea. Rev.*, **110**, 354–384, https://doi.org/10.1175/1520-0493(1982)110<0354:VITSST>2.0.CO;2.

Ray, S., and B. S. Giese, 2012: Historical changes in El Niño and La Niña characteristics in an ocean reanalysis. *J. Geophys. Res.*, **117**, C11007, https://doi.org/10.1029/2012JC008031.

Rogers, J. C., 1981: The North Pacific Oscillation. *J. Climatol.*, **1**, 39–57, https://doi.org/10.1002/joc.3370010106.

Smith, R. D., and Coauthors, 2010: The Parallel Ocean Program (POP) reference manual: Ocean component of the Community Climate System Model (CCSM) and Community Earth System Model (CESM). Los Alamos National Laboratory Tech. Rep. LAUR-10-01853, 141 pp., http://www.cesm.ucar.edu/models/cesm1.0/pop2/doc/sci/POPRefManual.pdf.

Thomas, E. E., and D. J. Vimont, 2016: Modeling the mechanisms of linear and nonlinear ENSO responses to the Pacific meridional mode. *J. Climate*, **29**, 8745–8761, https://doi.org/10.1175/JCLI-D-16-0090.1.

Tippett, M. K., A. G. Barnston, and S. Li, 2012: Performance of recent multimodel ENSO forecasts. *J. Appl. Meteor. Climatol.*, **51**, 637–654, https://doi.org/10.1175/JAMC-D-11-093.1.

Trenberth, K. E., 1997: The definition of El Niño. *Bull. Amer. Meteor. Soc.*, **78**, 2771–2777, https://doi.org/10.1175/1520-0477(1997)078<2771:TDOENO>2.0.CO;2.

Vimont, D. J., 2010: Transient growth of thermodynamically coupled variations in the tropics under an equatorially symmetric mean state. *J. Climate*, **23**, 5771–5789, https://doi.org/10.1175/2010JCLI3532.1.

——, D. S. Battisti, and A. C. Hirst, 2001: Footprinting: A seasonal connection between the tropics and mid-latitudes. *Geophys. Res. Lett.*, **28**, 3923–3926, https://doi.org/10.1029/2001GL013435.

——, ——, and ——, 2003a: The seasonal footprinting mechanism in the CSIRO general circulation models. *J. Climate*, **16**, 2653–2667, https://doi.org/10.1175/1520-0442(2003)016<2653:TSFMIT>2.0.CO;2.

——, J. M. Wallace, and D. S. Battisti, 2003b: The seasonal footprinting mechanism in the Pacific: Implications for ENSO. *J. Climate*, **16**, 2668–2675, https://doi.org/10.1175/1520-0442(2003)016<2668:TSFMIT>2.0.CO;2.

——, M. Alexander, and A. Fontaine, 2009: Midlatitude excitation of tropical variability in the Pacific: The role of thermodynamic coupling and seasonality. *J. Climate*, **22**, 518–534, https://doi.org/10.1175/2008JCLI2220.1.

Wang, B., R. Wu, and X. Fu, 2000: Pacific–East Asian teleconnection: How does ENSO affect East Asian climate. *J. Climate*, **13**, 1517–1536, https://doi.org/10.1175/1520-0442(2000)013<1517:PEATHD>2.0.CO;2.

Wang, F., 2010: Thermodynamic coupled modes in the tropical atmosphere–ocean: An analytical solution. *J. Atmos. Sci.*, **67**, 1667–1677, https://doi.org/10.1175/2009JAS3262.1.

Wen, C., A. Kumar, Y. Xue, and M. J. McPhaden, 2014: Changes in tropical Pacific thermocline depth and their relationship to ENSO after 1999. *J. Climate*, **27**, 7230–7249, https://doi.org/10.1175/JCLI-D-13-00518.1.

Wieners, C. E., H. A. Dijkstra, and W. P. M. de Ruijter, 2019: The interaction between the western Indian Ocean and ENSO in CESM. *Climate Dyn.*, **52**, 5153–5172, https://doi.org/10.1007/s00382-018-4438-2.

Wyrtki, K., 1985: Water displacements in the Pacific and the genesis of El Niño cycle. *J. Geophys. Res.*, **90**, 7129–7132, https://doi.org/10.1029/JC090iC04p07129.

Xie, S.-P., and S. G. H. Philander, 1994: A coupled ocean–atmosphere model of relevance to the ITCZ in the eastern Pacific. *Tellus*, **46A**, 340–350, https://doi.org/10.3402/tellusa.v46i4.15484.

Yeh, S.-W., J.-S. Kug, and S.-I. An, 2014: Recent progresses on two types of El Niño: Observations, dynamics, and future changes. *Asia-Pac. J. Atmos. Sci.*, **50**, 69–81, https://doi.org/10.1007/S13143-014-0028-3.

You, Y., and J. C. Furtado, 2017: The role of South Pacific atmospheric variability in the development of different types of ENSO. *Geophys. Res. Lett.*, **44**, 7438–7446, https://doi.org/10.1002/2017GL073475.

Yuan, X., 2004: ENSO-related impacts on Antarctic sea ice: A synthesis of phenomenon and mechanisms. *Antarct. Sci.*, **16**, 415–425, https://doi.org/10.1017/S0954102004002238.

Zhang, T., X. Shao, and S. Li, 2017: Impacts of atmospheric processes on ENSO asymmetry: A comparison between CESM1 and CCSM4. *J. Climate*, **30**, 9743–9762, https://doi.org/10.1175/JCLI-D-17-0360.1.

Zhou, Z.-Q., S.-P. Xie, X.-T. Zheng, Q. Liu, and H. Wang, 2014: Global warming–induced changes in El Niño teleconnections over the North Pacific and North America. *J. Climate*, **27**, 9050–9064, https://doi.org/10.1175/JCLI-D-14-00254.1.